

*Drivers of biases in the CMIP6  
extratropical storm tracks. Part II:  
Southern Hemisphere*

Article

Accepted Version

Priestley, M. D. K., Ackerley, D., Catto, J. L. and Hodges, K. I.  
ORCID: <https://orcid.org/0000-0003-0894-229X> (2021) Drivers  
of biases in the CMIP6 extratropical storm tracks. Part II:  
Southern Hemisphere. *Journal of Climate*, 36 (5). pp. 1469-  
1486. ISSN 1520-0442 doi: 10.1175/JCLI-D-20-0977.1  
Available at <https://centaur.reading.ac.uk/99467/>

It is advisable to refer to the publisher's version if you intend to cite from the  
work. See [Guidance on citing](#).

To link to this article DOI: <http://dx.doi.org/10.1175/JCLI-D-20-0977.1>

Publisher: American Meteorological Society

All outputs in CentAUR are protected by Intellectual Property Rights law,  
including copyright law. Copyright and IPR is retained by the creators or other  
copyright holders. Terms and conditions for use of this material are defined in  
the [End User Agreement](#).

[www.reading.ac.uk/centaur](http://www.reading.ac.uk/centaur)

**CentAUR**

Central Archive at the University of Reading

Reading's research outputs online

1 **Drivers of biases in the CMIP6 extratropical storm tracks. Part 2: Southern**  
2 **Hemisphere**

3 Matthew D. K. Priestley<sup>a</sup> Duncan Ackerley<sup>b</sup>, Jennifer L. Catto<sup>a</sup>, Kevin I. Hodges<sup>c,d</sup>

4 <sup>a</sup> *College of Engineering, Mathematics and Physical Sciences, University of Exeter, Exeter, UK*

5 <sup>b</sup> *Met Office, Exeter, UK*

6 <sup>c</sup> *Department of Meteorology, University of Reading, Reading, UK*

7 <sup>d</sup> *NCAS, Department of Meteorology, University of Reading, Reading, UK*

8 *Corresponding author: M. Priestley, m.priestley@exeter.ac.uk*

9 ABSTRACT: The Southern Hemisphere storm tracks are commonly simulated too far equatorward  
10 in climate models for the historical period. In the latest generation of climate models from the  
11 6th phase of the coupled model intercomparison project (CMIP6), the equatorward bias that was  
12 present in CMIP5 models still persists, although is reduced considerably. A further reduction of  
13 the equatorward bias is found in atmosphere-only simulations. Using diagnostic large-scale fields  
14 we propose that an increase in the midlatitude temperature gradients contributes to the reduced  
15 equatorward bias in CMIP6 and AMIP6 models, reducing the biases relative to ERA5. These  
16 changes increase baroclinicity in the atmosphere, and are associated with a storm track that is  
17 situated further poleward. In CMIP6 models, the poleward shift of the storm tracks is associated  
18 with an amelioration of cold midlatitude SST biases in CMIP5 and not through a reduction of  
19 the long-standing warm Southern Ocean SST bias. We propose that increases in midlatitude  
20 temperature gradients in the atmosphere and ocean are connected to changes in the cloud-radiative  
21 effect. Persistent track density biases to the south of Australia are shown to be connected to an  
22 apparent standing wave pattern originating in the tropics, which modifies the split jet structure near  
23 Australia and subsequently the paths of cyclones.

## 24 **1. Introduction**

25 Coupled climate models are the most sophisticated tools available for assessing potential  
26 changes to the climate in the coming century. The latest generation of models, part of the 6th  
27 phase of the coupled model intercomparison project (CMIP6; Eyring et al. 2016), represent  
28 the most recent scientific and computational advancements to help with this scientific goal. In  
29 order to assess future projections, models with a good fidelity in reproducing historical climate  
30 variability are required. However, climate models have been marred with considerable biases in  
31 relation to historical variability (e.g. Wang et al. 2014; Menary et al. 2015; Flato et al. 2013) and  
32 an understanding of the origins of these biases is required in order to determine deficiencies in,  
33 and future directions for, model development. In this study the drivers of biases in the Southern  
34 Hemisphere (SH) storm tracks are investigated. This study serves as a follow up to Priestley et al.  
35 (2020) and an accompaniment to the authors' investigation into drivers of Northern Hemisphere  
36 storm track biases (Priestley et al. 2022).

37  
38 Midlatitude cyclones, and the overall storm tracks, are vital components of the Earth's cli-  
39 mate system as they act to transfer heat and momentum polewards (Kaspi and Schneider 2013).  
40 They are also responsible for considerable amounts of midlatitude precipitation and extreme winds  
41 (e.g. Hawcroft et al. 2012; Dowdy and Catto 2017; Clark and Gray 2018). In previous generations  
42 of coupled climate models (e.g. CMIP3 and CMIP5; Meehl et al. 2007; Taylor et al. 2012), the  
43 storm track, and the general SH midlatitude circulation has tended to feature significant biases.  
44 These biases have mainly been apparent as an equatorward bias of the midlatitude circulation  
45 (Kidston and Gerber 2010; Chang et al. 2012, 2013), a zonal bias of the storm track in winter (Lee  
46 2015), and also an underestimation of cyclone intensity (Chang et al. 2013).

47  
48 In the CMIP6 models, the latitude of the SH storm track, and also the peak intensity of  
49 cyclones, is much improved and closely matches that of various reanalysis products relative to  
50 CMIP5 (Priestley et al. 2020). Furthermore, the mean SH midlatitude circulation has also shown  
51 clear improvements, with reductions in biases from CMIP3 through to CMIP5 (Bracegirdle et al.  
52 2013), and more recently in CMIP6, with the mean jet latitude in summer now being situated  
53 within  $0.5^\circ$  of that found in the latest fifth generation ECMWF reanalysis (ERA5, Bracegirdle

54 et al. 2020). It is not just the atmospheric circulation where improvements have been noted  
55 from CMIP5 to CMIP6. Improvements have been found in the surface temperature distribution,  
56 precipitation, ITCZ structure, and also the cloud radiative properties (Bock et al. 2020; Tian and  
57 Dong 2020), all of which may contribute to the reduction of storm track biases in CMIP6.

58  
59 The large equatorward bias in the SH circulation has been commonly linked to biases in  
60 SSTs and an underestimation of atmospheric temperature gradients across a number of generations  
61 of climate models (e.g. Trenberth and Fasullo 2010; Ceppi et al. 2012; Sallée et al. 2013; Wang  
62 et al. 2014). Recently, Garfinkel et al. (2020) linked the latitude of the eddy-driven jet to the  
63 representation of Aghulas Current, with models that have a weak Aghulas return current featuring  
64 a more equatorward jet. Two other recent studies (Curtis et al. 2020; Wood et al. 2020) have  
65 offered differing hypotheses as to why there has been a reduction in jet latitude bias from CMIP5  
66 to CMIP6. Curtis et al. (2020) discuss that it is a result of improvements in model resolution,  
67 whereas Wood et al. (2020) suggest that variations in SST are the leading driver of the change.

68  
69 Biases in Southern Ocean SST have been shown to be driven by biases in the atmospheric  
70 net surface shortwave flux (Hyder et al. 2018) resulting from the misrepresentation of cloud  
71 properties, specifically the shortwave cloud radiative effect (SWCRE; Ceppi et al. 2012; Grise and  
72 Polvani 2014). The SWCRE is commonly too weak, leading to a net heating of the SH. Biases  
73 in the SWCRE modify the strength of SST and midlatitude temperature gradients and hence  
74 hemispheric baroclinicity (Ceppi et al. 2012), but have also been shown to have an impact on  
75 the temperature structure of the atmosphere through radiative absorption (Li et al. 2015). These  
76 longstanding biases have been noted as an area for specific improvement for CMIP6 (Stouffer  
77 et al. 2017), as the shortwave cloud feedback has significant implications for the strength of the  
78 equilibrium climate sensitivity (Zelinka et al. 2020). So far several studies have demonstrated  
79 reduced biases in the newest model generations (Bock et al. 2020; Mauritsen et al. 2019; Kawai  
80 et al. 2019), however despite some reductions the CMIP6 multi-model mean has been shown to  
81 suffer from the same deficiencies as CMIP5 (Grise and Kelleher 2021).

82  
83 Another long-standing bias that has not improved from CMIP5 to CMIP6 is the positive

84 track density bias to the south of Australia (Priestley et al. 2020), which is associated with the  
85 split jet structure in this region and over New Zealand (Bals-Elsholz et al. 2001). The split jet is a  
86 feature that is simulated poorly in climate models, with an overly strong sub-tropical component,  
87 and a too weak polar component (Grose et al. 2016; Patterson et al. 2019). The representation  
88 of the split jet is partly driven by Antarctic orography (James 1988) and recently Patterson et al.  
89 (2020) linked the split jet bias in an idealized GCM to the representation of Antarctic orography  
90 affecting the eddy momentum fluxes in this region. Biases in the orographic wave drag have  
91 previously been linked to circulation biases in CMIP5 models (Pithan et al. 2016), as well as  
92 Rossby waves originating in the Indian Ocean which have been shown to alter the structure of the  
93 storm track to the south of Australia (Inatsu and Hoskins 2004, 2006).

94  
95 Understanding the origin of long-standing biases and reasons for their persistence is vital  
96 not just for future model development, but also for having confidence in model simulations and for  
97 understanding whether any systematic errors have an influence on future projections. The results  
98 presented herein aim to demonstrate linkages in the large-scale atmosphere-ocean system and to  
99 act as a framework for future scientific investigation. The science questions addressed in this study  
100 are as follows:

- 101 • Can the CMIP6 prescribed SST experiments (i.e. AMIP; Gates et al. 1999; Eyring et al. 2016)  
102 help to explain some of the coupled storm track biases in the SH?
  
- 103 • Can reduced storm track biases from CMIP5 to CMIP6 be associated with specific model  
104 developments?

105 The paper continues as follows. Section 2 describes the data and methods used for this work.  
106 Section 3 presents the results and findings. Finally, in section 4 the key points of this work and its  
107 implications in the wider scientific context will be discussed.

## 108 2. Data and Methods

### 109 a. Datasets

#### 110 1) CMIP6 MODELS

111 In this study the CMIP6 models covering the historical period are used. The *historical* and *amip*  
112 model runs are analyzed covering the period from 1979-2014. Focus will be on the December,  
113 January, February (DJF) and June, July, August (JJA) periods, representing the SH summer and  
114 winter seasons respectively. In total there are 24 models analyzed that have provided data from  
115 both a coupled atmosphere-ocean *historical* run and an atmosphere-only *amip* run for the required  
116 variables at 6-hourly temporal resolution. A full list of the models analyzed can be found in  
117 Table 1. The *amip* experiments are forced by observed SSTs and sea ice concentration and a  
118 full explanation of the differences between the experiments can be found in Eyring et al. (2016).  
119 Throughout this study the coupled models from the *historical* experiments will be referred to as  
120 the CMIP6 models, and the atmosphere-only models from the *amip* experiment will be referred to  
121 as the AMIP6 models. Monthly mean data are used to investigate biases in the large-scale fields.  
122 For all models only a single ensemble member (*rli1p1f1* or lowest available) is analyzed.

123

124 In some instances models will be separated between those of high and low resolution, for  
125 both the atmospheric and oceanic component. For the atmospheric resolution separation the  
126 distinction of Priestley et al. (2020) is used and models with a nominal atmospheric resolution  
127 (see Taylor et al. 2017) of 100 km are classed as 'high' resolution and those of 250 km are 'low'  
128 resolution.

#### 129 2) CMIP5 MODELS

130 The CMIP5 models, which are the same as those used in Priestley et al. (2020) (see also Table  
131 S1), provide a benchmark for the CMIP6 models. Of the 26 coupled CMIP5 models employed for  
132 this analysis, 19 of them have corresponding *amip* runs. For all models data is used covering the  
133 period 1979-2005. Tests have been performed using the 1979-2005 period for the CMIP6 models,  
134 with no discernible differences found compared to the data period described above. As with the

135 CMIP6 models, the coupled models will commonly be referred to as the CMIP5 models, with the  
 136 atmosphere-only variants being referred to as the AMIP5 models.

Model Name	Institution	Atmospheric Resolution	
		Horizontal	Vertical
ACCESS-CM2	CSIRO-ARCCSS; Commonwealth Scientific and Industrial Research Organisation, Australian Research Council Centre of Excellence for Climate System Science, Australia	N96; 192×144; 250km	85 levels to 85 km
ACCESS-ESM1-5	CSIRO; Commonwealth Scientific and Industrial Research Organisation, Australia	N96; 192×144; 250km	85 levels to 85 km
BCC-CSM2-MR	BCC; Beijing Climate Center, China	T206; 320×160; 100km	46 levels to 1.46 hPa
CMCC-CM2-HR4	CMCC; Fondazione Centro Euro-Mediterraneo sui Cambiamenti Climatici, Italy	288×192; 100km	26 levels to ~2 hPa
CMCC-CM2-SR5	CMCC; Fondazione Centro Euro-Mediterraneo sui Cambiamenti Climatici, Italy	288×192; 100km	30 levels to ~2 hPa
CNRM-CM6-1-HR	CNRM-CERFACS, Center National de Recherches Meteorologiques, center Européen de Recherche et de Formation Avancée en Calcul Scientifique, France	T359; 720×360; 100km	91 levels to 78.4km
EC-Earth3	EC-Earth-Consortium	TL255; 512×256; 100km	91 levels to 0.01 hPa
EC-Earth3-Veg	EC-Earth-Consortium	TL255; 512×256; 100km	91 levels to 0.01 hPa
GFDL-CM4	NOAA-GFDL; National Oceanic and Atmospheric Administration, Geophysical Fluid Dynamics Laboratory, USA	C96; 360×180; 100km	33 levels to 1 hPa
HadGEM3-GC3.1-LL	MOHC; Met Office Hadley Centre, UK	N96; 192×144; 250km	85 levels to 85 km
HadGEM3-GC3.1-MM	MOHC; Met Office Hadley Centre, UK	N216; 432×324; 100km	85 levels to 85 km
IPSL-CM6A-LR	IPSL; Institut Pierre Simon Laplace, France	N96; 144×143; 250km	79 levels to 40 km
KACE-1-0-G	NIMS-KMA; National Institute of Meteorological Sciences/Korea Meteorological Administration, Republic of Korea	N96; 192×144; 250km	85 levels to 85 km
KIOST-ESM	KIOST; Korea Institute of Ocean Science and Technology, Republic of Korea	C48; 192×96; 250km	32 levels to 2 hPa
MIROC-ES2L	MIROC; MIROC Consortium (JAMSTEC, AORI, NIES, R-CCS), Japan	T42; 128×64; 500km	40 levels to 3 hPa
MIROC6	MIROC; MIROC Consortium (JAMSTEC, AORI, NIES, R-CCS), Japan	T85; 256×128; 250km	81 levels to 0.004 hPa
MPI-ESM1-2-HR	MPI-M, DWD, DKRZ; Max Planck Institute for Meteorology, Deutscher Wetterdienst, Deutsches Klimarechenzentrum, Germany	T127; 384×192; 100km	95 levels to 0.01 hPa
MPI-ESM1-2-LR	MPI-M, AWI; Max Planck Institute for Meteorology, Alfred Wegener Institute, Germany	T63; 192×96; 250km	47 levels to 0.01 hPa
MRI-ESM2-0	MRI; Meteorological Research Institute, Japan	TL159; 320×160; 100km	80 levels to 0.01 hPa
NESM3	NUIST; Nanjing University of Information Science and Technology, China	T63; 192×96; 250km	47 levels to 1 hPa
NorESM2-LM	NCC; NorESM Climate Modelling Consortium, Norway	144×90; 250km	32 levels to 3 hPa
SAM0-UNICON	SNU; Seoul National University, Republic of Korea	288×192; 100km	30 levels to ≈2 hPa
TaiESM1	AS-RCEC; Research Center for Environmental Changes, Academia Sinica, Taiwan	288×192; 100km	30 levels to ≈2 hPa
UKESM1-0-LL	UKESM Consortium (MOHC, NERC, NIMS-KMA, NIWA)	N96; 192×144; 250km	85 levels to 85 km

137 TABLE 1. List of CMIP6/AMIP6 models that have been used in this study. Columns 3 and 4 indicate the  
 138 horizontal and vertical resolution of the atmospheric component of the model. Any spectral models are first stated  
 139 by their truncation type and number. 'T' stands for triangular truncation, 'TL' stands for triangular truncation  
 140 with linear Gaussian grid. The models with 'C' refers to a cubed-sphere finite volumes model, with the following  
 141 number being the number of grid cells along the edge of each cube face. Models with 'N' refer to the total  
 142 number of 2 grid point waves that can be represented in the zonal direction. Following any grid specification is  
 143 the dimensions of the model output on a gaussian longitude x latitude grid. The resolution stated in kilometres  
 144 is the stated nominal resolution of the atmospheric component of the model from Taylor et al. (2017).

### 145 3) REANALYSIS

146 As a reference to real-world atmospheric variability, the ERA5 reanalysis (Hersbach et al. 2020)  
 147 is used for comparison with the CMIP5 and CMIP6 models. ERA5 data spans the period from  
 148 January 1979 up to the near present, with the period 1979-2014 used to provide a consistent  
 149 comparison period for the CMIP6/AMIP6 models. The ERA5 data are output at  $0.28^\circ \times 0.28^\circ$   
 150 ( $\sim 31$  km) spatial resolution. Data are used at various output frequencies with feature tracking run  
 151 on 6-hourly vorticity fields and monthly-to-seasonal averages used for other large scale fields (see  
 152 below). For ERA5 and the CMIP5 and CMIP6 models described above, all large-scale analyses  
 153 are performed on the native grids that the data are provided on, the data is then interpolated onto a

154  $1^\circ \times 1^\circ$  grid for the purposes of visualization.

155

156 There are of course differences between numerous reanalysis products with regards to the  
157 storm tracks (Hodges et al. 2011) and other large-scale atmospheric variables (e.g. Mooney et al.  
158 2011; Trenberth et al. 2011; Lindsay et al. 2014). Newer generation reanalysis products have been  
159 shown to be more consistent in their state of the storm track (Priestley et al. 2020), and therefore  
160 in most instances only ERA5 will be used as a reference. However, for a more comprehensive  
161 estimation of the real-world cyclogenesis rate and cyclogenesis latitude, both the MERRA2  
162 (Gelaro et al. 2017) and JRA-55 (Kobayashi et al. 2015) reanalyses have been employed alongside  
163 ERA5 for the same time period.

#### 164 4) CERES

165 In calculations of the shortwave cloud radiative effect (SWCRE) the Clouds and the Earth's  
166 Radiant Energy System (CERES) Energy Balanced and Filled (EBAF) Top-of-Atmosphere (TOA)  
167 Edition-4.0 Data Product (Loeb et al. 2018) is used to validate the CMIP5 and CMIP6 data. Due  
168 to the reduced availability of CERES data and overlap with model data, this data set is analyzed in  
169 monthly mean format covering the period 2000 through 2014.

#### 170 *b. Feature Tracking*

171 For the identification and tracking of cyclones the method of Hodges (1995, 1999) is used. This  
172 method uses 850 hPa relative vorticity as the input variable, which allows for a reduced influence  
173 of the background state on cyclonic features and focuses on smaller spatial scales. The relative  
174 vorticity field is first truncated to T42 resolution with all planetary wavenumbers (5 and below)  
175 removed. This ensures tracking and cyclone identification is performed on a common resolution  
176 despite the varying input resolutions of the model data and reanalysis. Cyclones are initially  
177 identified as minima on a polar stereographic projection that exceed  $1 \times 10^{-5} \text{s}^{-1}$  (intensity scaled  
178 by -1). Following completion of the tracking cyclones are retained that travel at least 1000 km and  
179 have a lifetime of at least 48 hours. This ensures the focus is on long-lived and mobile synoptic  
180 systems.

181

182 Cyclone track density is calculated using spherical non-parametric estimators from the in-  
183 dividual cyclone tracks (Hodges 1996). In cases where cyclone genesis and lysis latitude are  
184 quantified this is taken as the latitude of the first and last (respective) timestep that the cyclone is  
185 identified. For determining the poleward propagation of cyclones the latitude difference between  
186 the 9th and 1st timestep (first 48 hours of lifecycle) of the cyclone track is taken.

### 187 *c. Metrics*

188 To further explore the large-scale climate of the CMIP models a number of diagnostics are used  
189 which require manipulation of the raw model output. These metrics are the same as in Priestley  
190 et al. (2022) and are documented below.

#### 191 1) TEMPERATURE GRADIENTS

192 Temperature gradients are calculated using the potential temperature ( $\theta$ ) on pressure levels.  
193 Gradients that are used are the meridional gradient of potential temperature as calculated by the  
194 Iris package (Met Office 2010 - 2013) and gradients are quoted in units of  $\text{K degree}^{-1}$ .

#### 195 2) STATIC STABILITY

196 The static stability is quantified in terms of the Brunt-Väisälä frequency ( $N^2$ ) calculated on  
197 pressure levels (equation 1).

$$N^2 = \frac{-pg^2}{RT\theta} \frac{d\theta}{dp} \quad (1)$$

198 The static stability is calculated for the lower troposphere with  $N^2$  covering the 700-850 hPa  
199 layer.  $T$  and  $\theta$  are the 700-850 hPa average temperature and potential temperature respectively.  $\frac{d\theta}{dp}$   
200 is the vertical gradient in  $\theta$ , calculated across the 700-850 hPa layer.

#### 201 3) EADY GROWTH RATE

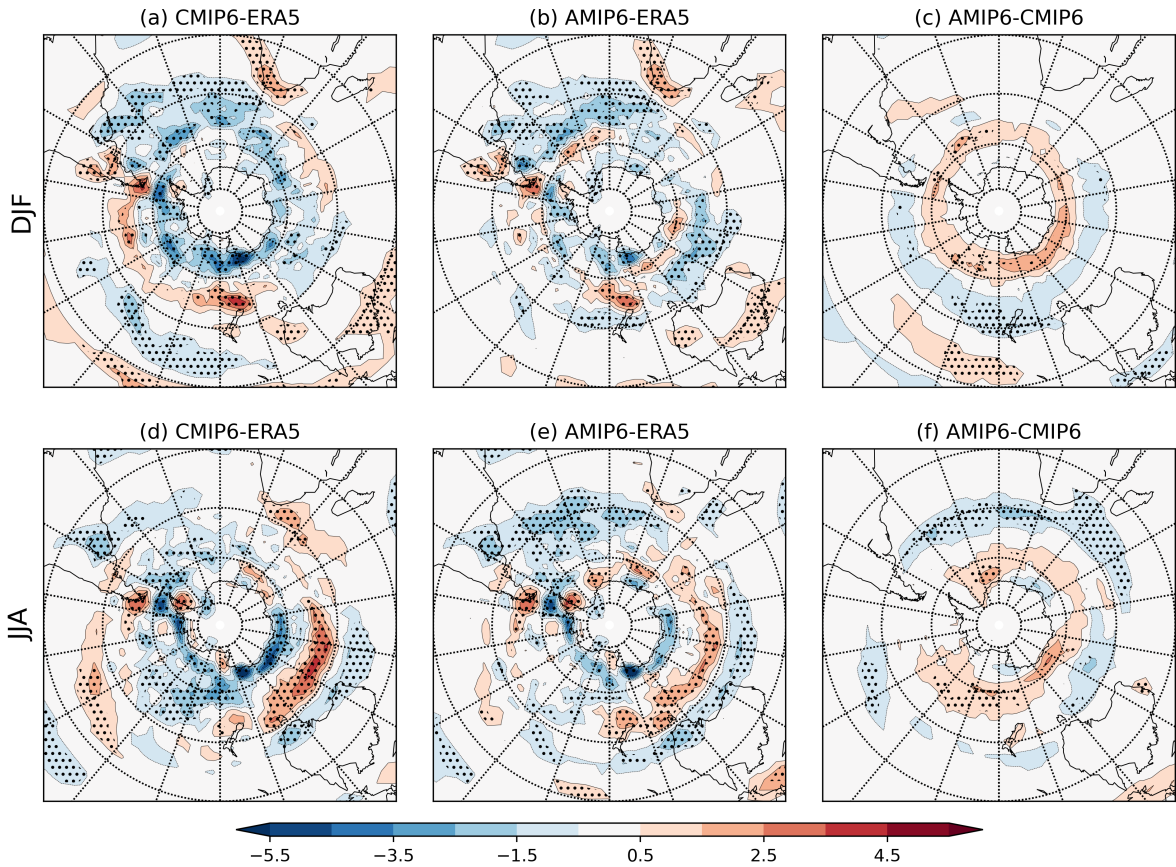
202 The Eady Growth Rate (EGR) is a description of the baroclinicity of the atmosphere and  
203 combines the two diagnostics described above. For this work the EGR will be a measure of the  
204 lower tropospheric baroclinicity and is defined in equation 2.

$$EGR = 0.31 f \frac{\left| \frac{\partial T}{\partial y} \right|}{\sqrt{N^2}} \quad (2)$$

205 The temperature gradient  $\left( \left| \frac{\partial T}{\partial y} \right| \right)$  is calculated at 850 hPa and the static stability ( $N^2$ ) is calculated  
 206 for the 700-850 hPa layer as detailed in equation 1.

### 207 3. Results

#### 208 a. Cyclone Track Densities and Statistics



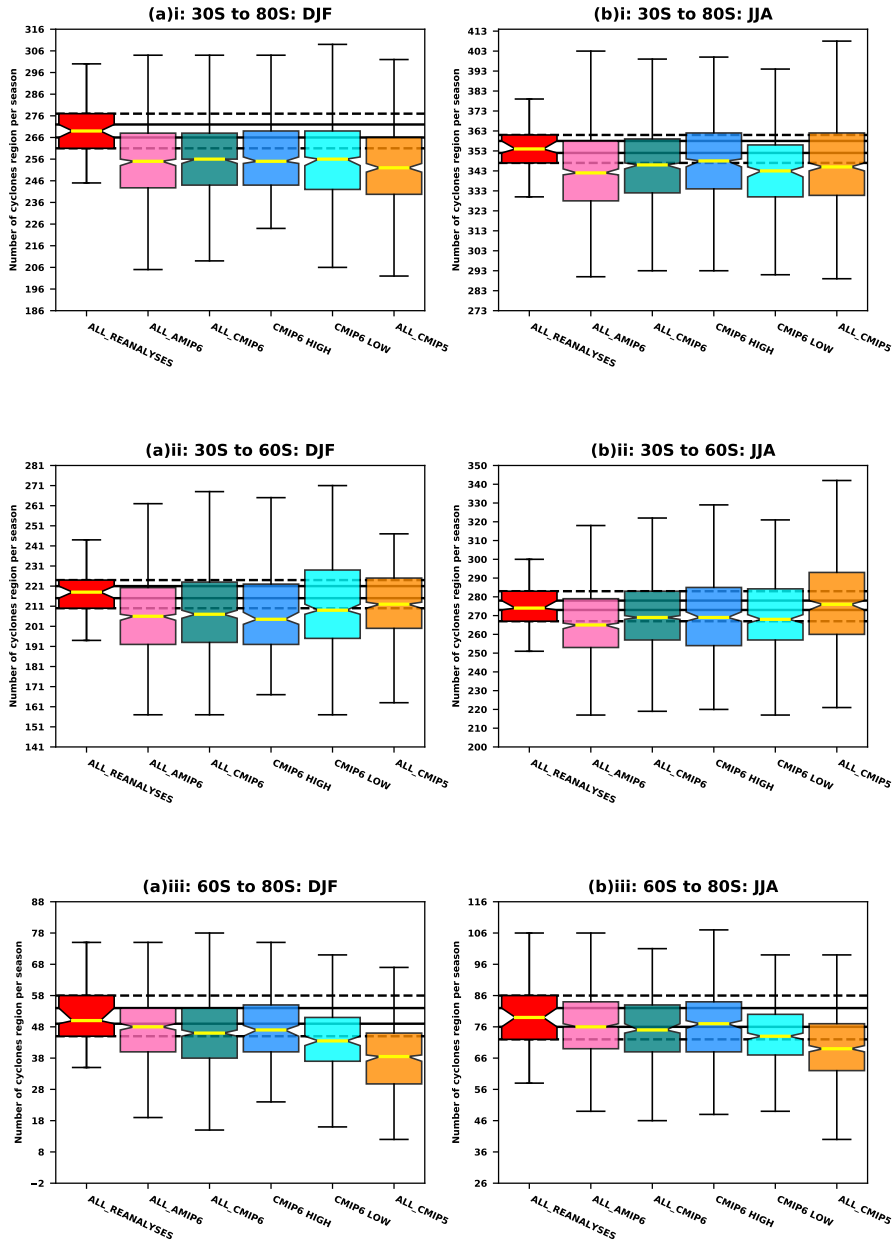
209 FIG. 1. Track density biases for DJF (a–c) and JJA (d–f) for (a,d) CMIP6 models and (b,e) AMIP6 models  
 210 relative to ERA5. (c,f) CMIP6-AMIP6. Units are number of cyclones per  $5^\circ$  spherical cap per month. Stippling  
 211 indicates where more than 80% of models agree on the sign of the error.

212 In the CMIP6 models, a general improvement in the representation of the SH storm tracks,  
 213 relative to ERA5, is seen when compared with CMIP5, particularly in DJF (Priestley et al.

214 2020). Priestley et al. (2020) found that the large equatorward storm track bias of CMIP5 is  
215 reduced in CMIP6, with a near total elimination of this feature. Similar patterns are seen in JJA,  
216 with a reduction in the equatorward bias noted, however some features still persist, such as an  
217 overestimation of track density to the south of Australia where cyclone tracks are too zonal.

218  
219 Track density biases for the 24 CMIP6 and AMIP6 models are shown in Fig. 1. During  
220 DJF, biases in the CMIP6 models (Fig. 1a) are almost identical to those analyzed in Priestley  
221 et al. (2020) and indicate an underestimation of tracks in DJF and a slight equatorward bias  
222 relative to ERA5. In the AMIP6 models (Fig. 1b) the pattern of biases relative to ERA5 is  
223 generally consistent with CMIP6, however there is a poleward shift in the track density (Fig. 1c).  
224 Consequently, the previous most evident equatorward biases in DJF across the South Pacific and  
225 to the south of New Zealand are mostly eradicated in AMIP6.

226  
227 The poleward shift of the track density in the AMIP6 models relative to CMIP6 is re-  
228 flected in the regional cyclogenesis rates (Fig. 2a). During DJF the genesis rate for the whole  
229 SH (Fig. 2a) in the AMIP6 models has a very similar median to the CMIP6 models (255 and  
230 256 cyclones per season respectively, not significantly different, Table S2), with slightly larger  
231 inter-model spread. The similar genesis rate for the whole hemisphere can be broken down to  
232 slightly lower rates of genesis in the equatorward sector (30°S-60°S) and higher rates in the  
233 poleward sector (60°S-80°S) in the AMIP6 models relative to CMIP6 (Figs. 2a(ii-iii)). Despite  
234 these differences, the genesis density biases (relative to ERA5) are similar between AMIP6 and  
235 CMIP6 (Fig. S1d). Some of the differences in genesis density help explain the differences in  
236 track density between AMIP6 and CMIP6, for example, there is a reduction in cyclogenesis over  
237 New Zealand (Fig. S1d), which is co-located with a reduction in track density (and subsequent  
238 poleward shift of tracks, Fig. 1c).



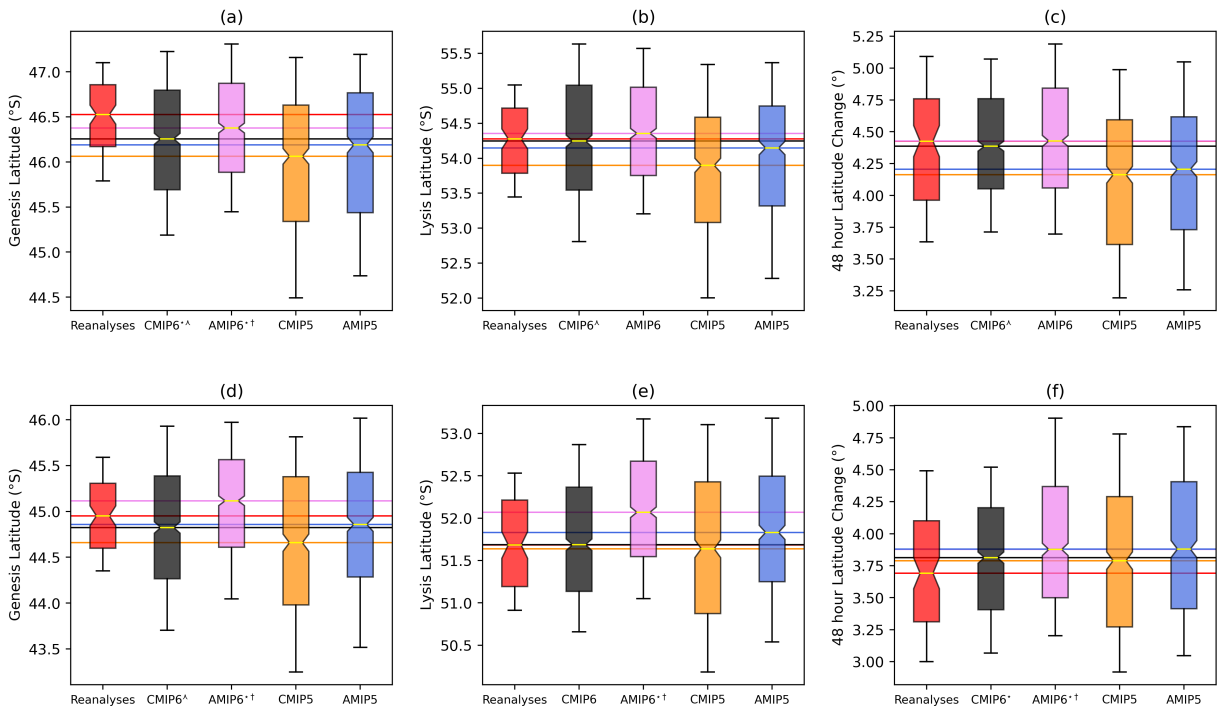
239 FIG. 2. Boxplots of regional cyclogenesis rates for (a) DJF and (b) JJA. Results are shown for all reanalyses,  
 240 AMIP6, CMIP6, the two resolution groups of CMIP6, and CMIP5. Solid black lines indicate the uncertainty  
 241 range of the reanalyses median and dashed black lines signify the 25th-75th percentile range of the reanalyses.  
 242 Boxes extend to the 25th and 75th percentile respectively with yellow lines indicating the distribution median.  
 243 Notches around the median show the uncertainty estimate based on 10,000 random samples and whiskers extend  
 244 to the 10th and 90th percentiles.

245 The median location of cyclogenesis during DJF in ERA5 and the model groups are plotted in  
246 Fig 3a. All model groups are biased by up to  $0.5^\circ$  equatorward relative to the reanalyses, with  
247 CMIP5 being the most biased. The CMIP6 models simulate genesis further poleward than CMIP5  
248 by  $\sim 0.2^\circ$  ( $p < 0.05$ ), with AMIP6 another  $0.1^\circ$  further poleward, although both are still biased  
249 significantly equatorward relative to the reanalyses. The lysis latitude is well simulated by the  
250 CMIP6 and AMIP6 models (Fig. 3b), however the CMIP5 models simulate lysis significantly too  
251 equatorward according to this metric. Finally, the poleward displacement of cyclones is also well  
252 represented in the CMIP6 and AMIP6 models relative to the reanalyses (Fig. 3c). The CMIP5  
253 and AMIP5 simulations tend to underestimate the poleward displacement in the first 48 hours of  
254 the cyclone lifecycle by  $\sim 0.25^\circ$ , which is significantly lower than the CMIP6 models. Across  
255 all measures the CMIP6/AMIP6 models perform better than the CMIP5/AMIP5 models, with a  
256 poleward shift in AMIP relative to CMIP. This suggests that the large improvement seen in track  
257 density and the representation of the storm tracks shown in Priestley et al. (2020) has occurred  
258 through model developments from CMIP5 to CMIP6. Despite the similarities, there is a larger  
259 poleward shift from CMIP5-CMIP6 than from AMIP5-AMIP6, with shifts of  $0.48^\circ$  and  $0.43^\circ$   
260 respectively in lifetime average latitude.

261  
262 In the winter season (JJA), a similar pattern of track density biases in the CMIP6 and  
263 AMIP6 models is evident (Fig. 1d–f). However, the highest track density, as in DJF, is improved  
264 in AMIP6 through a poleward shift relative to CMIP6 (Fig. 1f). Other features such as the overly  
265 high track density to the southeast of South Africa are reduced. The persistent overestimation  
266 of tracks to the south of Australia in the CMIP6 models (as described in Priestley et al. 2020) is  
267 also present in the AMIP6 models, although to a lesser extent. Therefore, it is likely that this bias  
268 depends upon both the atmosphere/land components of the models and is being amplified through  
269 the coupling to an interactive ocean.

270  
271 In JJA the AMIP6 models also have lower genesis rates than the CMIP6 models from  
272  $30^\circ\text{S}$ - $60^\circ\text{S}$  (Fig. 2b(ii)) and higher genesis rates from  $60^\circ\text{S}$ - $80^\circ\text{S}$  (Fig. 2b(iii)). Overall, there are  
273 significantly ( $p < 0.05$ ) fewer cyclones in JJA in AMIP6 models compared to CMIP6 (medians of  
274 342 and 346 cyclones per season respectively; Fig. 2b(i)). In JJA there is an underestimation of

275 track density from the east coast of South America along 40°S toward South Africa in AMIP6  
 276 relative to CMIP6 (Fig. 1f), which represents an even larger underestimation of track density  
 277 relative to ERA5. This underestimation of track density is coincident with a robust underestimation  
 278 of genesis density (Fig. S1h). Interestingly, there are minimal differences in genesis rate to the  
 279 south of Australia in either CMIP6 or AMIP6 relative to ERA5, or from CMIP6 to AMIP6 (Figs.  
 280 S1f–h). This suggests that the robust track density bias in this region (Fig. 1d,e) is unrelated to  
 281 the number of cyclones and instead may be driven by errors in cyclone paths being too zonal.



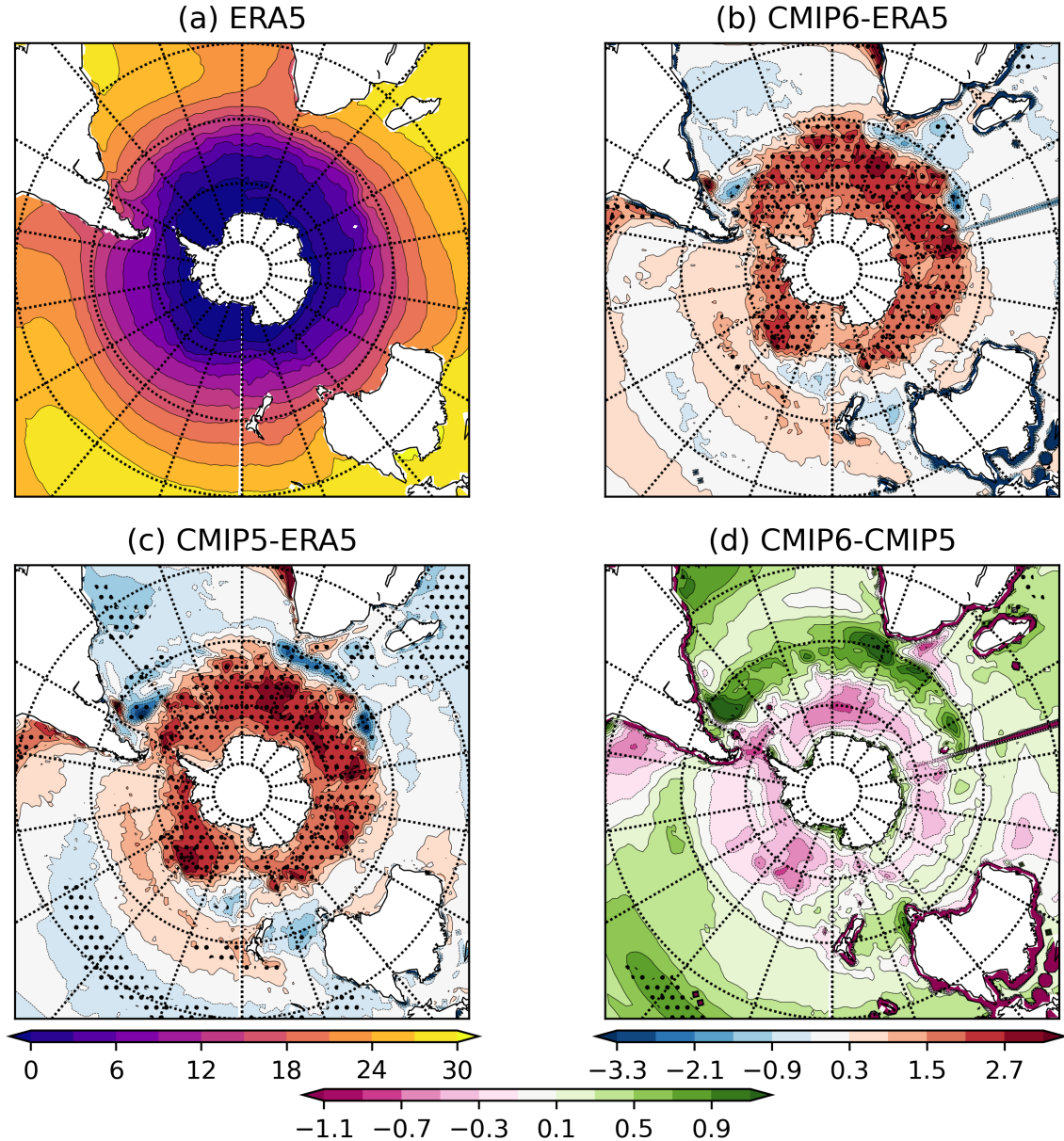
282 FIG. 3. Boxplots of annual mean cyclogenesis latitude (a,d), cyclolysis latitude (b,e), and cyclone 48-hour  
 283 latitude change (c,f) for Reanalyses, CMIP6, AMIP6, CMIP5, and AMIP5 in DJF (a–c) and JJA (d–f). Horizontal  
 284 coloured lines indicate the median value for each model distribution. Boxes extend to the 25th and 75th percentile  
 285 respectively with yellow lines indicating the distribution median. Notches around the median show the uncertainty  
 286 estimate based on 10,000 random samples and whiskers extend to the 10th and 90th percentiles. In the labels  
 287 ★ indicates where the model group is significantly different from the reanalyses, † indicates where AMIP6  
 288 and CMIP6 are significantly different, and λ indicates where CMIP6 and CMIP5 are significantly different.  
 289 Significance tests performed using a Mood’s Median test and quoted at the 5% level.

290 In JJA the differences in genesis latitude, lysis latitude, and cyclone poleward movement between  
291 the CMIP5, CMIP6, and their AMIP counterparts is similar to DJF (Figs. 3d–f). The median  
292 genesis latitude continues to be biased equatorward in CMIP5 and CMIP6, although genesis in  
293 CMIP6 occurs significantly further poleward than CMIP5, with less than half the bias. The  
294 cyclogenesis latitude is displaced significantly poleward in AMIP6 relative to CMIP6, which  
295 agrees with Figs. 1 and 2, although the genesis latitude in the AMIP6 models is  $\sim 0.1^\circ$  poleward  
296 of the reanalyses (Fig. 3d). The lysis latitude is very well represented in CMIP5 and CMIP6,  
297 with a continued poleward bias in AMIP6 relative to ERA5 (Fig. 3e). Finally, for the poleward  
298 displacement of the cyclones, all model groups perform similarly but are biased with up to  $\sim 0.2^\circ$   
299 more poleward movement than the reanalyses (Fig. 3f). For most of the metrics in Fig. 3d–f  
300 the models produce good results relative to the reanalyses and, at all times, there is considerable  
301 overlap in their inter-quartile ranges.

### 302 *b. Poleward Shift of the Storm Tracks*

306 The largest change from CMIP5 to CMIP6 is the large improvement in the latitudinal bias of  
307 the storm track (particularly for DJF) leading to a storm track that is almost unbiased in latitude  
308 relative to ERA5 (Priestley et al. 2020; Bracegirdle et al. 2020; Curtis et al. 2020). The drivers of  
309 this improvement from CMIP5 to CMIP6, and the further reduction in the bias in AMIP6 models,  
310 will be explored below.

312 In DJF there is a large positive SST bias around Antarctica in the CMIP6 models (Fig.  
313 4b) relative to ERA5 (Fig. 4a), which has persisted from CMIP5 (Fig. 4c). The SST biases in  
314 Fig. 4 are substantially different than those shown in OMIP experiments (Tsujino et al. 2020),  
315 indicating it is likely that the SST biases are driven by processes occurring in the atmospheric  
316 component of the models. For CMIP5 models, the warm bias in the high latitude Southern  
317 Ocean has been demonstrated to arise from positive biases in the cloud-related shortwave fluxes,  
318 which result in associated errors in atmospheric net heat flux (Ceppi et al. 2012; Hyder et al.  
319 2018). These biases have been shown to be linked to insufficient cloudiness and optical depth  
320 within the cold sectors of cyclones (Grise and Polvani 2014; Williams et al. 2013; Bodas-Salcedo  
321 et al. 2014; Govekar et al. 2014; Williams and Bodas-Salcedo 2017). As the CMIP6 models

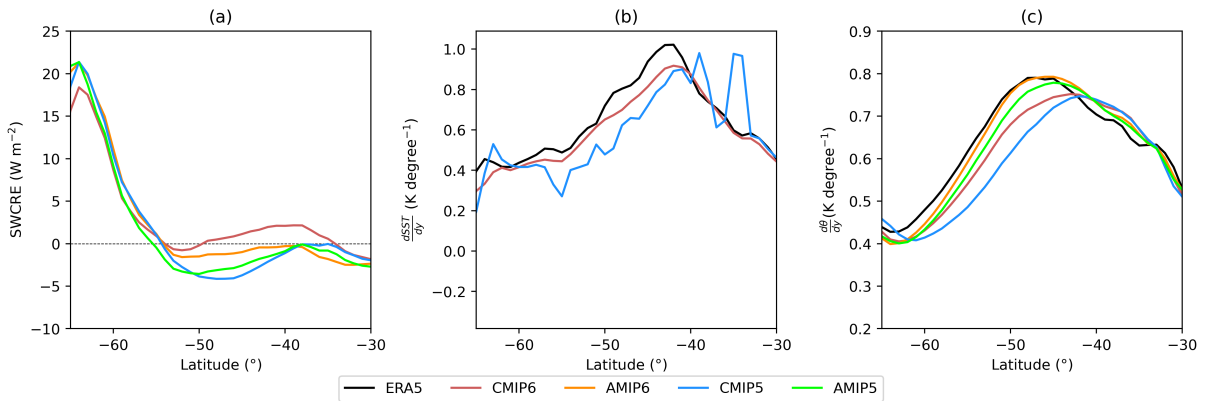


303 FIG. 4. DJF averaged sea surface temperature (SST) for (a) ERA5 (b) CMIP6-ERA5, (c) CMIP5-ERA5, and  
 304 (d) CMIP6-CMIP5. Stippling indicates where there is 80% model agreement on the sign of the bias. Units are  
 305 °C. Data are taken from the Sea Surface Temperature (*tos*) CMIP variable.

322 continue to have a high-latitude Southern Ocean that is too warm relative to observations, it is  
 323 likely that the same biases in the cloud-related shortwave fluxes are still present. To demonstrate  
 324 this the zonal mean differences in the SWCRE for CMIP6 (red line) and CMIP5 (blue line)

325 relative to CERES are plotted in Fig. 5a. In the CMIP6 models the SWCRE is still too weak<sup>1</sup>  
 326 relative to CERES at high latitudes (i.e. poleward of 55°S, red line in Fig. 5a), and therefore  
 327 the process driving the warm SSTs in the CMIP5 models appears unimproved in the CMIP6 models.

328  
 329 At mid-to-lower latitudes (from approximately 40°S-50°S) CMIP6 SSTs are generally up  
 330 to 1°C higher than in CMIP5 (Fig. 4d), particularly in the South Atlantic and Indian Ocean  
 331 sectors. The SSTs in this sector are particularly important for modulating the latitude of the storm  
 332 track in CMIP6 models (as indicated by the significant linear regression in Fig. 6a), with warmer  
 333 SSTs associated with a more poleward storm track. This is not something that is seen in CMIP5  
 334 models (Fig. 6b). This 40°S-50°S latitude band is where the largest differences in the magnitude  
 335 of the SWCRE bias from CMIP5 to CMIP6 are seen, with CMIP6 models having a smaller bias  
 336 and less negative SWCRE compared to CMIP5 (Fig. 5a). This reduced bias is likely contributing  
 337 to the higher midlatitude SSTs in CMIP6. It is worth noting here that the increase in SSTs (CMIP6  
 338 relative to CMIP5) is largely the result of the amelioration of cold biases present in the CMIP5  
 339 models (particularly in the region of the Agulhas current retroflexion, see Fig. 4).



340 FIG. 5. The ensemble zonal mean difference in (a) SWCRE ( $\text{W m}^{-2}$ ), (b) zonal mean SST gradient ( $\text{K degree}^{-1}$ ) and (c) zonal mean 850 hPa potential temperature gradient ( $\text{K degree}^{-1}$ ) for CMIP6 (red line),  
 341 AMIP6 (orange line), CMIP5 (blue line) and AMIP5 (green line). The differences are for (a) model ensemble  
 342 mean minus CERES.  
 343

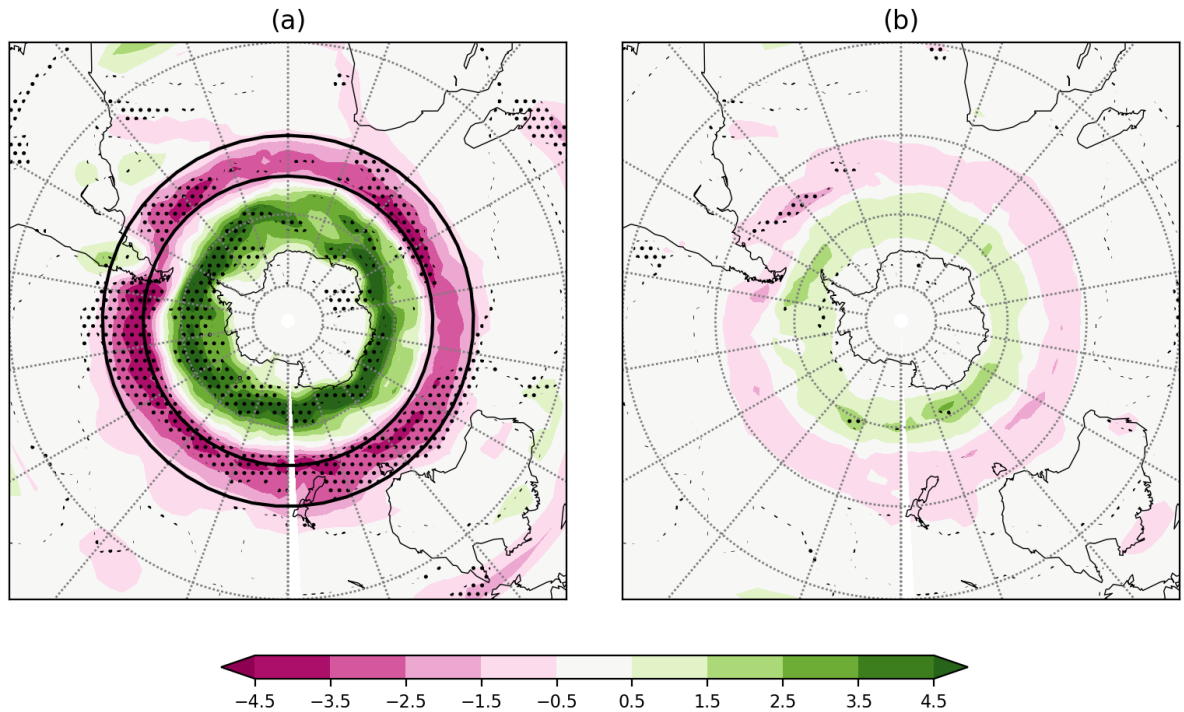
<sup>1</sup>as the "background state" SWCRE is negative in both the models and CERES, a positive bias implies that CMIP6 SWCRE is "less negative" (i.e. weaker) than that of CERES and vice versa

344 The pattern of positive high-latitude and negative midlatitude SST biases in CMIP6 and CMIP5  
345 (discussed above) causes the SST gradient to be weaker poleward of 40°S in both ensembles  
346 relative to ERA5 (Fig. 5b). Nevertheless, the midlatitude SST gradient in CMIP6 is stronger than  
347 CMIP5 between approximately 40°S-60°S (see Fig. 5b). A good representation of the strong SH  
348 midlatitude SST gradient in the models is important as it acts to maintain baroclinicity in the  
349 atmosphere (Nakamura et al. 2008; Nakayama et al. 2021). A weak temperature gradient may  
350 reduce the midlatitude baroclinicity and thereby reduce the strength of the storm track (Graff and  
351 LaCasce 2014; Garfinkel et al. 2020; Kajtar et al. 2021; Nakayama et al. 2021). It is therefore  
352 important to evaluate whether the biases in the SST gradient (Fig. 5b) are also apparent in the  
353 atmosphere. The zonal mean 850 hPa potential temperature ( $\theta_{850}$ ) gradient is plotted for ERA5  
354 (black line), CMIP5 (blue line) and CMIP6 (red line) in Fig. 5c. The CMIP6 and CMIP5 models  
355 generally feature a weaker atmospheric temperature gradient in the midlatitudes relative to ERA5  
356 (Fig. 5c) as a result of temperatures being too high surrounding Antarctica. As with the SST  
357 gradient, the biases in the  $\theta_{850}$  gradient are smaller in CMIP6 than CMIP5, relative to ERA5. The  
358 stronger  $\theta_{850}$  gradient in CMIP6 relative to CMIP5 between 40°S-60°S (Fig. 5c, red versus blue  
359 lines) is likely to be driven by the higher  $\theta_{850}$  values equatorward of approximately 50°S rather  
360 than the (smaller magnitude) reduction in 850 hPa  $\theta$  adjacent to Antarctica (Fig. S3e).

361  
362 In order to further evaluate the role of the SST biases on the atmospheric temperature gra-  
363 dient and storm tracks, data from the AMIP6 simulations are used. As the SSTs in AMIP6  
364 simulations are prescribed from observations, the biases in the midlatitude SST gradient should be  
365 negligible and any errors should be primarily the result of atmospheric processes. In the AMIP6  
366 models, a stronger  $\theta_{850}$  gradient is seen compared to CMIP6 models (Fig. 5c, orange versus  
367 red lines), although the  $\theta_{850}$  gradients are weaker relative to ERA5 poleward of 50°S (Fig. 5c,  
368 black line). The larger midlatitude temperature gradient in AMIP6 is the likely driver of the more  
369 poleward location of the storm track relative to CMIP6 (see Fig. 1c and Priestley et al. 2020)  
370 and the largest increases in the 850 hPa zonal wind (Fig. S2c). The increase in  $\theta_{850}$  gradient in  
371 AMIP6 relative to CMIP6 is driven by reducing the high latitude temperature bias (Fig. S3c) and  
372 not through increasing lower latitude temperatures, as is the case from CMIP5 to CMIP6 (Fig.  
373 S3e). Nevertheless, there are still clearly biases in the representation of the SH storm track in

374 the AMIP6 simulation (Fig. 1c), which are not resolved by using observed SSTs. Moreover, as  
375 both the AMIP5 and AMIP6 models are forced by the same prescribed SSTs, there should be  
376 minimal influence from the ocean state and therefore one would not expect large differences in the  
377 midlatitude temperature gradient. However, there is a clear increase in the temperature gradient in  
378 AMIP6 models, relative to AMIP5 (Fig. 5c). This increase in temperature gradient is associated  
379 with higher temperatures in the lower troposphere from 40°-50°S in similar locations to the biases  
380 in the coupled models (black contours Fig. S3e and f). Radiative processes have been shown to  
381 influence the temperature structure of atmosphere-only models (Li et al. 2015) and, as with the  
382 coupled models, the AMIP6 models feature a smaller bias in SWCRE than the AMIP5 models  
383 in the midlatitudes (40°-50°S, Fig. 5a). The temperature (and gradient) change from AMIP5 to  
384 AMIP6 is geographically very similar to the CMIP5 to CMIP6 change, yet is smaller in magnitude.  
385 Therefore, the temperature change from 40°S-50°S has its origins in the atmospheric component  
386 of the models, which is then amplified further by the SST biases in the coupled models (as in  
387 Hyder et al. 2018).

388  
389 Overall there has been an improvement in the SH midlatitude temperature gradients (both  
390  $\theta_{850}$  and SST) from CMIP5 to CMIP6 (Figs. 5b and 5c). This improvement appears to be  
391 the result of reducing biases in the SWCRE in the midlatitudes (Fig. 5a). Furthermore, when  
392 SSTs are prescribed from observations (AMIP6), the representation of the temperature gradients  
393 improve further. These results (SST and  $\theta_{850}$  gradient improvement) are consistent with the better  
394 representation of the storm tracks in CMIP6 relative to CMIP5 (also noted by Bracegirdle et al.  
395 2020), and also AMIP6 relative to CMIP6. There is also a clear improvement of the temperature  
396 gradient (Fig. 5c) and jet (Fig. S2f) in AMIP6 relative to AMIP5, despite both experiments using  
397 the same SST dataset (as also noted by Curtis et al. 2020). Therefore, improvements in the SST  
398 alone cannot explain the improved midlatitude circulation in CMIP6 relative to CMIP5. However,  
399 while the location of the jet and mean latitude of cyclogenesis (Fig. 2a) are simulated better in  
400 CMIP6/AMIP6 relative to CMIP5/AMIP5, there is still a lack of cyclogenesis events (Fig. 1a and  
401 Table S2) in the SH during DJF. Therefore there are still clear problems with the representation of  
402 extratropical cyclones in the SH midlatitudes. Further interpretation is given in Section 4.



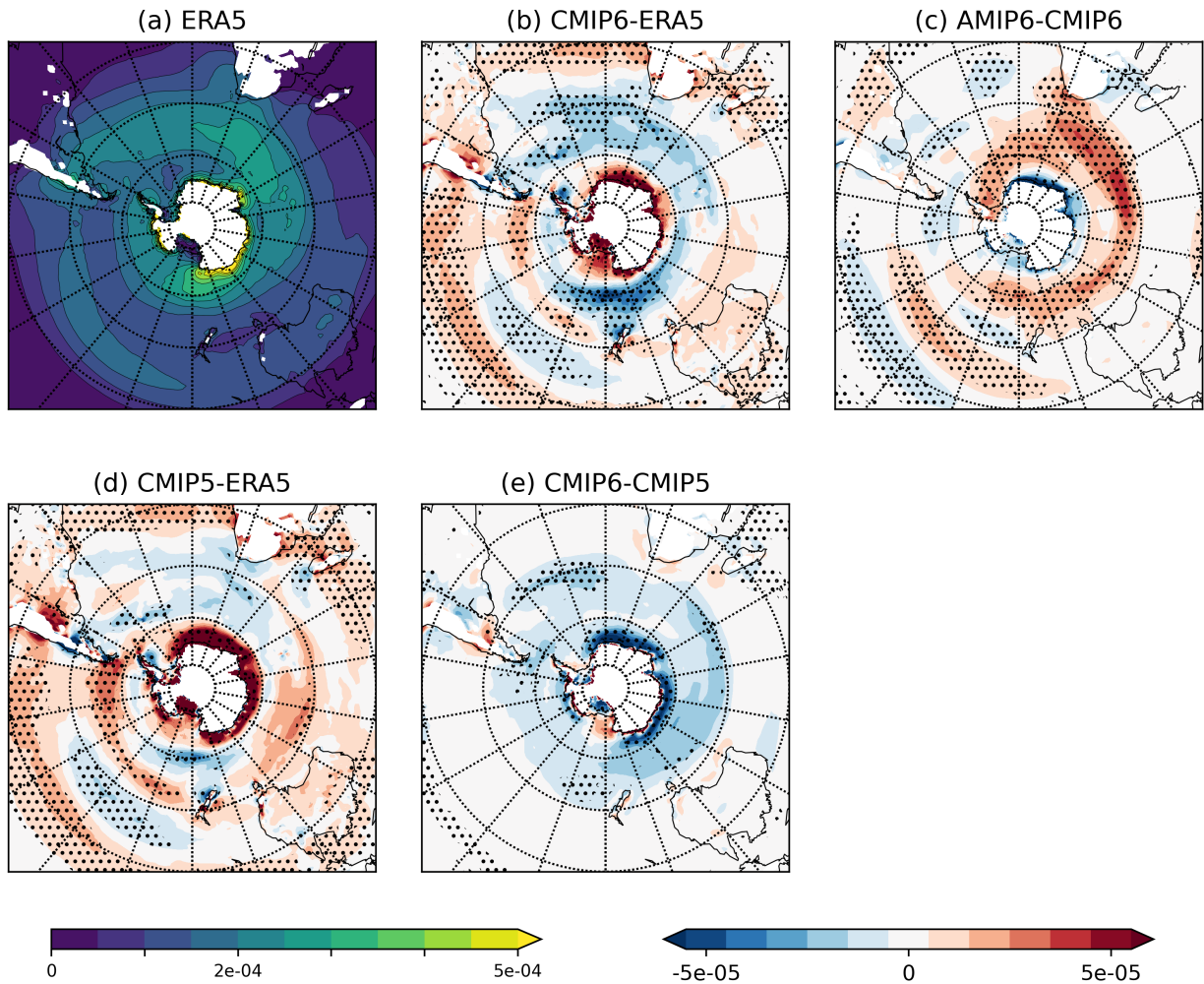
403 FIG. 6. Linear least-squares grid-point regression slope maps of DJF seasonal mean storm track density, against  
 404 area averaged SST from 40°S-50°S for (a) CMIP6 and (b) CMIP5. Regression is performed across the model  
 405 means of the CMIP6 and CMIP5 ensembles respectively. Stippling indicates where regressions are significant  
 406 at the 5% level. The black box in (a) indicates the region of SSTs used in the regression calculations. Units are  
 407 cyclones per month  $K^{-1}$ .

### 408 *c. Winter Cyclogenesis Rate*

409 Despite improvements in modeling capabilities from CMIP5 to CMIP6, CMIP6 models continue  
 410 to underestimate cyclogenesis rate in the SH (Fig. 2b). Unlike in DJF, radiative processes do  
 411 not have a dominant influence on baroclinicity and therefore the cyclogenesis rate and storm track  
 412 latitude in JJA. Consequently, we use the Eady Growth Rate (EGR) to examine rates of cyclogenesis  
 413 in the SH winter. The EGR broadly indicates where the largest track and genesis densities are  
 414 likely to occur. Positive (negative) EGR biases are a proxy for higher (lower) cyclone track and  
 415 genesis densities.

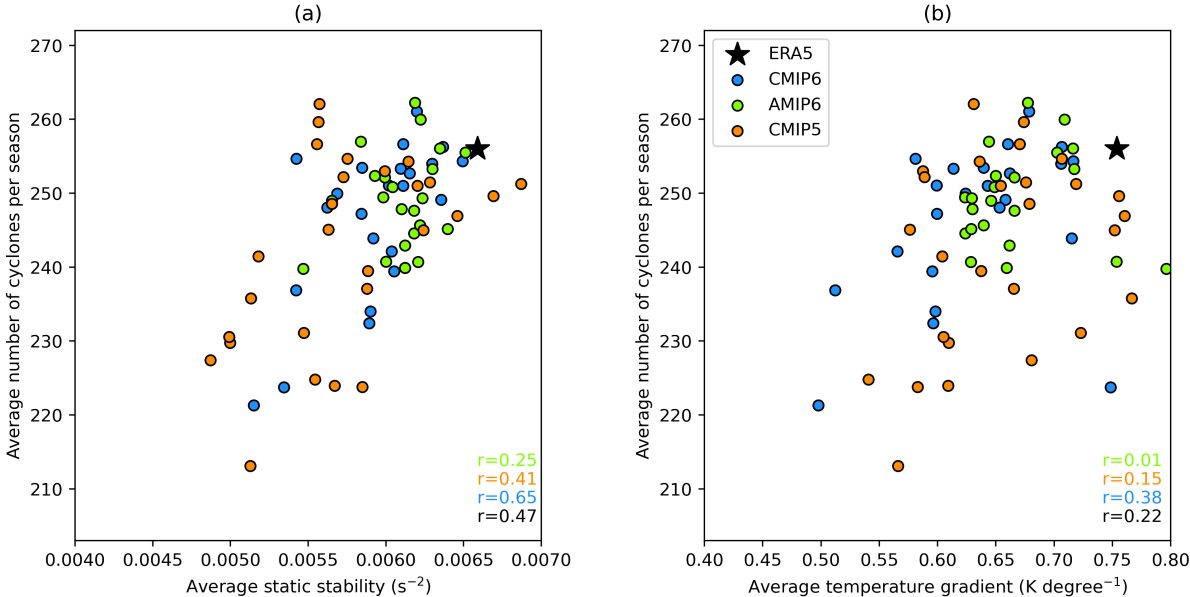
416 1) EADY GROWTH RATE

417 In JJA the CMIP6 models feature negative biases of EGR in the South Atlantic sector and to the  
 418 south of New Zealand and generally higher values around the rest of the hemisphere (Fig. 7b),  
 419 with a similar pattern of biases in CMIP5 (Fig. 7d). However, the CMIP6 models tend to have  
 420 lower EGR values around a majority of the SH, relative to CMIP5 (Fig. 7e). The smaller EGR of  
 421 CMIP6 is consistent with the lower cyclogenesis rate in CMIP6 relative to CMIP5, equatorward of  
 422 60°S (Fig. 2b). In the AMIP6 models the EGR is higher than in CMIP6 (Fig. 7c), which is not  
 423 consistent with the cyclogenesis rate (Fig. 2b).



424 FIG. 7. Eady Growth Rate for JJA for (a) ERA5, (b) CMIP6-ERA5, (c) AMIP6-CMIP6, (d) CMIP5-ERA5,  
 425 and (e) CMIP6-CMIP5. Units are  $s^{-1}$ . Stippling indicates where there is 80% model agreement on the sign of  
 426 the change.

427 The differences in EGR, and the related cyclogenesis rates can be understood through inspecting  
 428 the two components that make up the EGR, the gradient of potential temperature at 850 hPa and  
 429 the lower tropospheric static stability (see equation 2). For both CMIP5 and CMIP6, a positive  
 430 relationship is seen between the average static stability from 40°S-70°S and the rate of cyclogenesis  
 431 in the same region (Fig. 8a). Furthermore, these two fields are positively correlated, which implies  
 432 that models that are more stable have higher levels of cyclogenesis. This is counter-intuitive as  
 433 cyclogenesis will typically occur in less stable environments. Reducing the lower-tropospheric  
 434 stability through an imposed 4K surface heating would not change the temperature gradient, and  
 435 a lower stability does not appear to influence the cyclogenesis rate in the models (Fig. 8a). It  
 436 therefore seems unlikely that the static stability is the driving factor behind the lack of cyclogenesis  
 437 in the CMIP6 models.



438 FIG. 8. Scatter plots of (a) lower tropospheric static stability ( $s^{-2}$ ) and (b) 850 hPa potential  
 439 temperature gradient ( $K \text{ degree}^{-1}$ ) against seasonal cyclogenesis rate. Large-scale fields are averages from 40°S-70°S for  
 440 CMIP6 (blue), CMIP5 (orange), AMIP6 (green) and ERA5 (black star) in JJA.

441 The other component of the EGR is the potential temperature gradient associated with vertical  
 442 wind shear. All model groups, both CMIP and AMIP feature a positive relationship between the  
 443  $\theta_{850}$  gradient and number of cyclones (Fig. 8b), with models that have more cyclones having a  
 444 stronger temperature gradient. Unlike the stability relationships, this is what would be expected,

445 as stronger temperature gradients that more closely match the reanalysis values would result in a  
446 greater number of cyclones. Therefore, it appears that the strength of the temperature gradient,  
447 and not the atmospheric stability, is the primary factor controlling the cyclogenesis rate.

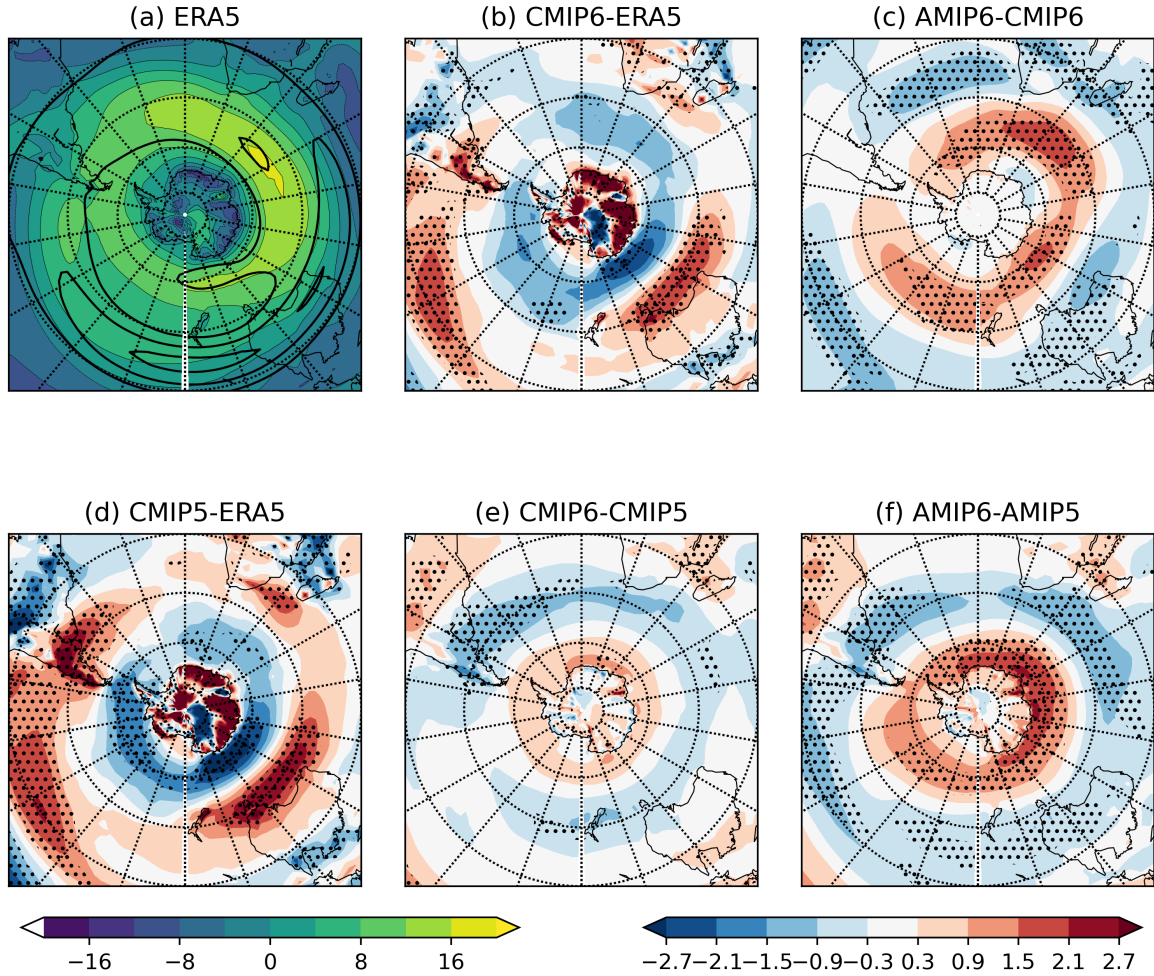
448  
449 This result also suggests that correcting the cause of SST biases in coupled models might  
450 improve the stability of the models, but as the stability does not appear to be the controlling factor  
451 on cyclogenesis rate, this may not yield any additional cyclogenesis. However, a decrease in SSTs  
452 in the most poleward regions would also increase the large-scale temperature gradient (as in Fig.  
453 S3c), and therefore increase the rate of cyclogenesis.

#### 454 *d. Persistent South Australian Track Density Overestimation*

455 One bias that has persisted from CMIP5 to CMIP6, and is also present in the AMIP6 models  
456 (Fig. 1d–f), is the overestimation of the track density to the south of Australia during JJA. This  
457 bias is associated with the bifurcation of the split sub-tropical and polar front jet located in  
458 this region (Fig. 9), which models represent poorly (Grose et al. 2016; Patterson et al. 2019).  
459 Models tend to have biases from  $\sim 90^{\circ}\text{E}$ – $180^{\circ}\text{E}$  with a too strong subtropical jet along  $40^{\circ}\text{S}$   
460 (most visible at 250 hPa, Fig. S5a), and a polar jet that is too weak along  $60^{\circ}\text{S}$  (most visible  
461 at 850 hPa, Fig. 9a). Despite the two jets generally being identified at different pressure levels,  
462 the two biases are notable in the CMIP6 and CMIP5 models (Fig. 9b,d, S5b–d) at all pressure levels.  
463  
464  
465

466  
467 The bias in the zonal wind reflects that of the track density bias of CMIP6 models in Fig.  
468 1d–f and also of CMIP5 models in Fig. 9 of Priestley et al. (2020). The CMIP6 models simulate  
469 only a slight poleward shift in the zonal wind south of Australia (Fig. 9e), as in the track density,  
470 relative to CMIP5. The AMIP6 models feature a more poleward circulation than in CMIP6 (Fig.  
471 9c), although the zonal bias in this sector still remains (not shown), suggesting that this error may  
472 be amplified by SST biases in the coupled models, but ultimately has its roots in the atmosphere  
473 or land component of the models.

474  
475 The better representation of the jet and storm track structure in AMIP6 is a result of a  
476 more poleward location of the circulation in JJA relative to CMIP6 (similar but smaller magnitude



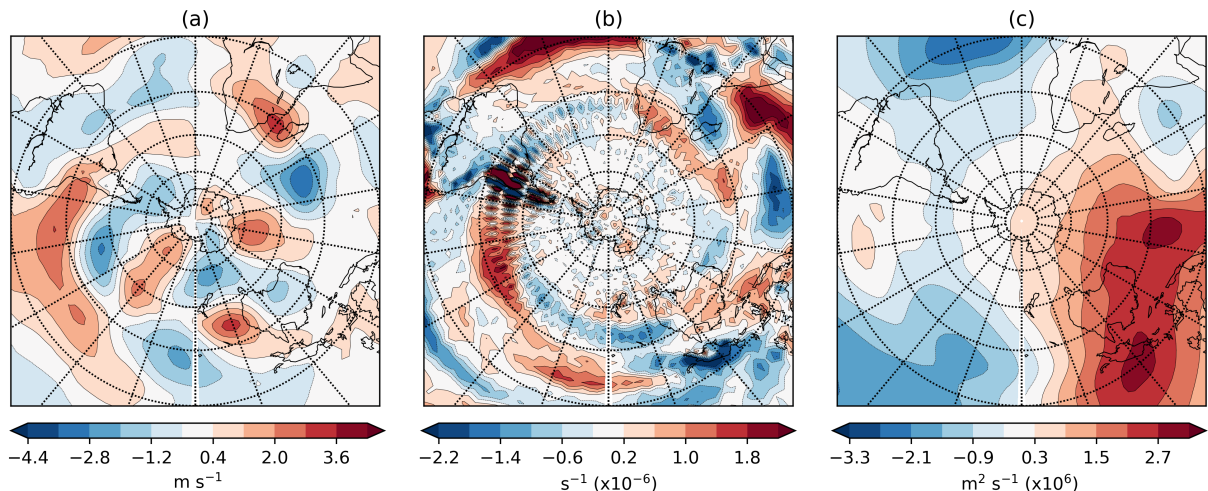
455 FIG. 9. JJA averaged zonal wind ( $u$ ) at 850 hPa for (a) ERA5, (b) CMIP6-ERA5, (c) AMIP6-CMIP6, (d)  
 456 CMIP5-ERA5, (e) CMIP6-CMIP5, and (f) AMIP6-AMIP5. Overlaid black contours in (a) is the 250 hPa ERA5  
 457 zonal wind with contours of 24, 36, and 48  $\text{m s}^{-1}$ .

477 as discussed in Bracegirdle et al. 2020). In JJA the SST anomalies of the CMIP6 models are  
 478 consistent with those in DJF (Fig. 4) and therefore the AMIP6 models have considerably lower  
 479 atmospheric potential temperature relative to CMIP6 (south of South Africa, poleward of  $50^\circ\text{S}$ )  
 480 when the SSTs are corrected (Fig. S6c). This decrease in potential temperature poleward of  
 481  $50^\circ\text{S}$  leads to an increase in the temperature gradient from  $40^\circ\text{S}$ - $50^\circ\text{S}$  in AMIP6 relative to  
 482 CMIP6 in a very similar pattern to the increase in EGR shown in Fig. 7c from  $20^\circ\text{W}$ - $100^\circ\text{W}$ . The  
 483 stronger temperature gradient contributes to shifting the circulation poleward, which may then  
 484 have downstream impacts on the South Australian sector. Despite this shift, the dominant split

485 jet bias clearly still has an impact on the circulation and track density bias of this region in the  
486 AMIP6 models.

487

488 The driver of the positive bias in the zonal wind from 100°E-160°E cannot be directly in-  
489 vestigated due to the limited output of CMIP6 models and inability to perform interactive  
490 experiments, however insight can be gained through examination of the seasonal mean meridional  
491 wind ( $v$ ) which appears to display an anomalous standing wave pattern in the CMIP6 models (Fig.  
492 10). Directly to the west of the zonal jet anomaly (Fig. 9b) there is a region of anomalously  
493 northwards (positive  $v$ ) motion (along 100°E; Fig. 10a) which contributes to reducing the  
494 poleward motion of cyclones downstream of the anomaly. There also appears to be a wave train  
495 (denoted by the opposing meridional wind anomalies) extending in an arc from Madagascar to the  
496 west coast of South America (Fig. 10a). The origins of this apparent wave train can be estimated  
497 from biases in the divergence and velocity potential (Fig. 10b,c). To the southeast of the horn of  
498 Africa, positive divergence, and negative velocity potential (relative to ERA5), indicates a possible  
499 source of this standing wave pattern.



500 FIG. 10. Circulation biases of CMIP6 relative to ERA5 for (a) meridional wind, (b) divergence, and (c) velocity  
501 potential. All variables are shown at 250 hPa and for JJA.

502 The presence of the split jet has been shown to be associated with Rossby waves originating  
503 from upper-level divergence over the Indian Ocean (Inatsu and Hoskins 2004, 2006) and it has  
504 been shown that Rossby wave sources are incorrectly modeled in the CMIP5 models (Nie et al.

505 2019). Based on the divergence pattern and origin of the wave train it is also possible that this  
506 wave train could have its origins in the equatorial Atlantic ocean, where biases in the location  
507 of the ITCZ (present in CMIP6 models, see Tian and Dong 2020), affect the source of planetary  
508 waves. Divergence anomalies across southern Africa could also be a result of incorrect orographic  
509 interaction with the mean-flow, which is a long standing problem with GCMs (Inatsu and Hoskins  
510 2004). Recently, Patterson et al. (2020) associated the split-jet bias to the representation of Antarctic  
511 orography, and therefore the incorrect representation of the orographic impact on the circulation in  
512 the CMIP6 models may be contributing to this bias. The stationary wave pattern in the meridional  
513 wind, the divergence, and velocity potential is evident in all models and also in the atmosphere-only  
514 simulations for both 5th and 6th generation models.

#### 515 **4. Discussion and Conclusions**

516 In this study the state of the Southern Hemisphere storm tracks has been examined in both coupled  
517 and atmosphere-only model simulations from both the 5th and 6th Coupled Model Intercomparison  
518 Projects. The influence of ocean biases on model errors and also other large-scale features has been  
519 investigated. Furthermore, reasons for improvements from CMIP5 to CMIP6 have been explored.  
520 The main conclusions of this work are detailed below.

- 521 • AMIP6 models generally show reduced storm track biases relative to CMIP6 models (Fig. 1).  
522 AMIP6 models also tend to simulate storm tracks that are located further poleward than in  
523 CMIP6, eliminating some of the equatorward bias relative to ERA5 (Fig. 2, 3). Despite these  
524 improvements, the overall cyclogenesis rate is biased even lower than CMIP6 (Fig. 2).
- 525 • The improved location of the storm track due to a poleward shift from CMIP5 to CMIP6 is  
526 associated with increased SSTs and temperatures in the lower troposphere from 40°S-50°S  
527 (Fig. 4, S3), which increases the midlatitude temperature gradients (Fig. 5, S3). The AMIP6  
528 models simulate an improvement of the storm track location relative to the AMIP5 models  
529 due to increases in the tropospheric temperature with no influence from the underlying ocean  
530 state (Fig. 5c).
- 531 • The biases in cyclogenesis rates in the SH are primarily associated with increases in atmo-  
532 spheric temperature gradients rather than static stability (Fig. 8). Models that have lower

533 cyclogenesis rates relative to reanalyses have midlatitude temperature gradients that are too  
534 weak.

- 535 • The overestimation of tracks to the south of Australia in JJA is related to biases in the split jet  
536 in the same region, where the sub-tropical jet is too strong. The jet appears to be modulated by  
537 a planetary wave train that likely has origins in the equatorial Indian and/or Atlantic Oceans,  
538 which weakens the polar component of the split jet (Fig. 10). The presence of the wave train  
539 decreases the poleward movement of cyclones forming to the southwest of Australia, driving  
540 the track density bias.

541 One finding from this work is that the CMIP6 models offer an improved representation of the  
542 storm track latitude compared to CMIP5 as a result of a poleward shift in temperature gradients  
543 and jet latitude. However, despite this apparent improvement, the shift in temperature gradients  
544 and circulation appears to be driven by an amelioration of pre-existing CMIP5 biases, particularly  
545 in the region of the Agulhas current retroflexion, and not through improving the long-standing  
546 high latitude Southern Ocean warm biases. Therefore, further attention is required to eliminate  
547 these compensating biases that may yield further improvements in storm track representation and  
548 have implications for future projections (Kajtar et al. 2021).

549  
550 With respect to the improvement in the representation of the latitude of maximum zonal  
551 wind and cyclogenesis in CMIP6 relative to CMIP5, we have explored three plausible reasons for  
552 this:

- 553 1. The representation of SSTs within the models, particularly with respect to their variability and  
554 geographical distribution of warm and cold areas, are driving the changes in the SH circulation  
555 in CMIP6 relative to CMIP5 (Wood et al. 2020).
- 556 2. Increased resolution in the CMIP6/AMIP6 generation of models, relative to their  
557 CMIP5/AMIP5 counterparts, leads to the SH jet being located more poleward (i.e. better) in  
558 the higher resolution CMIP6/AMIP6 simulations (Curtis et al. 2020).
- 559 3. Improvements in the representation of clouds and their radiative properties within the models  
560 may lead to an improvement in the temperature structure of the whole atmosphere, which

561 leads to a better representation of the preferred location of baroclinic eddy growth. This has  
562 been shown in atmosphere-only models by Li et al. (2015).

563 It is clear from the analysis provided in Section 3a that it is difficult to truly separate the impact of  
564 SST (Wood et al. 2020), resolution (Curtis et al. 2020) and clouds (Li et al. 2015) on the preferred  
565 location for extratropical cyclone development and it is likely that each process is playing a role  
566 in causing errors in the SH storm tracks. Given the changes in the 850 hPa temperature gradient  
567 and the mean cyclogenesis latitude seen in the AMIP6 runs relative to AMIP5 (Figs. 5c and  
568 3a), it is more likely that the processes suggested by Curtis et al. (2020) and Li et al. (2015)  
569 (i.e. points 2 and 3 above) are likely to be the main causes. Nevertheless, there is some impact  
570 from the SST distribution (Fig. 5b and 6a), which agrees with Wood et al. (2020). Furthermore,  
571 the representation of other physical processes (either parametrised or explicitly represented) not  
572 discussed in the study may be contributing to the changes in mean state from CMIP5 to CMIP6.  
573 The representation of surface drag (Pithan et al. 2016), cloud radiative heating (Voigt and Shaw  
574 2015), and the resolution of the stratosphere (Wilcox et al. 2012) have all been shown to influence  
575 the mean state and response of the SH circulation. All these features likely influence the model  
576 biases, yet understanding which is playing the dominant role may be key to understanding the  
577 biases in extratropical cyclone formation in the SH; however, this is beyond the scope of this paper  
578 and is an area for future work.

579  
580 The atmospheric temperature gradient has been shown to be important for correctly repre-  
581 senting the cyclogenesis rate in the Southern Hemisphere (Fig. 8b). As the CMIP6 and  
582 AMIP6 models still tend to underestimate the cyclogenesis rate (Fig. 2) it is likely that  
583 improvements will be made with increased horizontal resolution. Increasing resolution would  
584 likely have beneficial impacts on SST and atmospheric temperature gradients and therefore  
585 storm track latitude and cyclogenesis rate, as was suggested by Curtis et al. (2020). However,  
586 resolution is not the only important factor when representing extratropical cyclones, which  
587 can be seen by comparing cyclogenesis rates in the midlatitude and high latitude bands  
588 (Fig. 2 and Priestley et al. 2020) and indicates that the low-resolution CMIP6 (~250 km)  
589 models perform similarly to the high-resolution (~100 km) CMIP6 models. Therefore, further  
590 work is needed to identify how resolution plays a role in improving the representation of the

591 storm tracks and whether that improvement might be negated by the configuration of a given model.

592

593 Going forward, further investigation into the drivers of the SH circulation and storm track  
594 biases can be performed utilizing the HighResMIP experiments (Haarsma et al. 2016). These  
595 models feature horizontal resolutions of  $\sim 25\text{-}50\text{km}$  and ocean resolutions of  $0.25^\circ$  and have  
596 yielded improvements in numerous global model biases (e.g. Baker et al. 2019; Gutjahr  
597 et al. 2019; Roberts et al. 2019). Despite the aforementioned limited improvements with  
598 horizontal atmospheric resolution of  $100\text{km}$  (Priestley et al. 2020), it may be that increases  
599 in resolution to  $25\text{-}50\text{km}$  in the HighResMIP models yields some benefits. Willison et al.  
600 (2013) noted improvements in cyclone moist processes at  $20\text{km}$  resolution, which can have  
601 feedbacks on large-scale circulation (e.g. Tamarin and Kaspi 2016). Furthermore, orographic  
602 features are more accurately represented in high resolution models (Sandu et al. 2019), and im-  
603 proved orographic representation has been shown to reduce circulation biases in the SH (Patterson  
604 et al. 2020) and NH (Davini et al. 2021), and may be significantly improved in HighResMIP models.

605

606 An additional research avenue would be to investigate the processes leading to the changes  
607 in radiative forcing in the latest generation of coupled and atmosphere-only models. Creating  
608 specific experiments from which a wide array of variables can be output, the influence from  
609 longwave and shortwave radiation and the rates of atmospheric absorption can be quantified.  
610 Finally, it has recently been documented by Kajtar et al. (2021) that models with reduced latitudinal  
611 biases have less 'capacity for change' under future climate conditions and that models with greater  
612 latitudinal storm track/jet biases have stronger climate responses (e.g. Chang et al. 2012; Kidston  
613 and Gerber 2010). Therefore, as the CMIP6 models in this study have a reduced equatorward bias,  
614 it may be that the magnitude of the poleward shift of storm tracks in the Southern Hemisphere is  
615 smaller in CMIP6 than in CMIP5.

616

617 *Acknowledgments.* M. D. K. Priestley and J. L. Catto are supported by the Natural Envi-  
618 ronment Research Council (NERC) grant NE/S004645/1. D. Ackerley was supported by the  
619 Met Office Hadley Centre Climate Programme funded by BEIS and Defra. K. I. Hodges  
620 was funded by the United Kingdom's Natural Environment Research Council (NERC) as part

621 of the National Centre for Atmospheric Science. We thank the ECMWF for their ERA5 re-  
622 analysis, which is available from the Copernicus Climate Change Service Climate Data Store  
623 (<https://cds.climate.copernicus.eu/#!/search?text=ERA5&type=dataset>). CMIP6 data is publicly  
624 available through the Earth System Grid Federation (<https://esgf-node.llnl.gov/projects/cmip6/>).  
625 We are very grateful to the three anonymous reviewers and the editor, whose comments greatly  
626 improved the quality of this manuscript.

## 627 **References**

- 628 Baker, A. J., and Coauthors, 2019: Enhanced Climate Change Response of Wintertime  
629 North Atlantic Circulation, Cyclonic Activity, and Precipitation in a 25-km-Resolution  
630 Global Atmospheric Model. *Journal of Climate*, **32** (22), 7763–7781, [https://doi.org/10.1175/  
631 JCLI-D-19-0054.1](https://doi.org/10.1175/JCLI-D-19-0054.1).
- 632 Bals-Elsholz, T. M., E. H. Atallah, L. F. Bosart, T. A. Wasula, M. J. Cempa, and A. R. Lupo,  
633 2001: The Wintertime Southern Hemisphere Split Jet: Structure, Variability, and Evolution.  
634 *Journal of Climate*, **14** (21), 4191–4215, [https://doi.org/10.1175/1520-0442\(2001\)014<4191:  
635 TWSHSJ>2.0.CO;2](https://doi.org/10.1175/1520-0442(2001)014<4191:TWSHSJ>2.0.CO;2).
- 636 Bock, L., and Coauthors, 2020: Quantifying Progress Across Different CMIP Phases With the  
637 ESMValTool. *Journal of Geophysical Research: Atmospheres*, **125** (21), e2019JD032321,  
638 <https://doi.org/https://doi.org/10.1029/2019JD032321>.
- 639 Bodas-Salcedo, A., and Coauthors, 2014: Origins of the Solar Radiation Biases over the  
640 Southern Ocean in CFMIP2 Models\*. *Journal of Climate*, **27** (1), 41–56, [https://doi.org/  
641 10.1175/JCLI-D-13-00169.1](https://doi.org/10.1175/JCLI-D-13-00169.1).
- 642 Bracegirdle, T. J., C. R. Holmes, J. S. Hosking, G. J. Marshall, M. Osman, M. Patterson,  
643 and T. Rackow, 2020: Improvements in Circumpolar Southern Hemisphere Extratropical  
644 Atmospheric Circulation in CMIP6 Compared to CMIP5. *Earth and Space Science*, **7** (6),  
645 e2019EA001065, <https://doi.org/https://doi.org/10.1029/2019EA001065>.
- 646 Bracegirdle, T. J., E. Shuckburgh, J.-B. Sallee, Z. Wang, A. J. S. Meijers, N. Bruneau, T. Phillips,  
647 and L. J. Wilcox, 2013: Assessment of surface winds over the Atlantic, Indian, and Pacific Ocean  
648 sectors of the Southern Ocean in CMIP5 models: historical bias, forcing response, and state  
649 dependence. *Journal of Geophysical Research: Atmospheres*, **118** (2), 547–562, [https://doi.org/  
650 https://doi.org/10.1002/jgrd.50153](https://doi.org/https://doi.org/10.1002/jgrd.50153).
- 651 Ceppi, P., Y.-T. Hwang, D. M. W. Frierson, and D. L. Hartmann, 2012: Southern Hemisphere  
652 jet latitude biases in CMIP5 models linked to shortwave cloud forcing. *Geophysical Research  
653 Letters*, **39** (19), <https://doi.org/10.1029/2012GL053115>.

654 Chang, E. K. M., Y. Guo, and X. Xia, 2012: CMIP5 multimodel ensemble projection of storm  
655 track change under global warming. *Journal of Geophysical Research: Atmospheres*, **117** (D23),  
656 <https://doi.org/10.1029/2012JD018578>.

657 Chang, E. K. M., Y. Guo, X. Xia, and M. Zheng, 2013: Storm-Track Activity in IPCC  
658 AR4/CMIP3 Model Simulations. *Journal of Climate*, **26** (1), 246–260, [https://doi.org/](https://doi.org/10.1175/JCLI-D-11-00707.1)  
659 [10.1175/JCLI-D-11-00707.1](https://doi.org/10.1175/JCLI-D-11-00707.1).

660 Clark, P. A., and S. L. Gray, 2018: Sting jets in extratropical cyclones: a review. *Quarterly Journal*  
661 *of the Royal Meteorological Society*, **144** (713), 943–969, [https://doi.org/https://doi.org/10.1002/](https://doi.org/https://doi.org/10.1002/qj.3267)  
662 [qj.3267](https://doi.org/https://doi.org/10.1002/qj.3267).

663 Curtis, P. E., P. Ceppi, and G. Zappa, 2020: Role of the mean state for the Southern Hemispheric  
664 jet stream response to CO2 forcing in CMIP6 models. *Environmental Research Letters*, **15** (6),  
665 <https://doi.org/10.1088/1748-9326/ab8331>.

666 Davini, P., F. Fabiano, and I. Sandu, 2021: Orographic resolution driving the improvements  
667 associated with horizontal resolution increase in the Northern Hemisphere winter mid-latitudes.  
668 *Weather and Climate Dynamics Discussions*, 1–25, <https://doi.org/10.5194/wcd-2021-51>.

669 Dowdy, A. J., and J. L. Catto, 2017: Extreme weather caused by concurrent cyclone, front and  
670 thunderstorm occurrences. *Scientific Reports*, **7**, <https://doi.org/10.1038/srep40359>.

671 Eyring, V., S. Bony, G. A. Meehl, C. A. Senior, B. Stevens, R. J. Stouffer, and K. E. Taylor,  
672 2016: Overview of the Coupled Model Intercomparison Project Phase 6 (CMIP6) experimental  
673 design and organization. *Geoscientific Model Development*, **9** (5), 1937–1958, [https://doi.org/](https://doi.org/10.5194/gmd-9-1937-2016)  
674 [10.5194/gmd-9-1937-2016](https://doi.org/10.5194/gmd-9-1937-2016).

675 Flato, G., and Coauthors, 2013: *Evaluation of Climate Models*, book section 2, 741–866. Cam-  
676 bridge University Press, Cambridge, United Kingdom and New York, NY, USA, [https://doi.org/](https://doi.org/10.1017/CBO9781107415324.020)  
677 [10.1017/CBO9781107415324.020](https://doi.org/10.1017/CBO9781107415324.020), URL [www.climatechange2013.org](http://www.climatechange2013.org).

678 Garfinkel, C. I., I. White, E. P. Gerber, and M. Jucker, 2020: The Impact of SST Biases in  
679 the Tropical East Pacific and Agulhas Current Region on Atmospheric Stationary Waves in  
680 the Southern Hemisphere. *Journal of Climate*, **33** (21), 9351–9374, [https://doi.org/10.1175/](https://doi.org/10.1175/JCLI-D-20-0195.1)  
681 [JCLI-D-20-0195.1](https://doi.org/10.1175/JCLI-D-20-0195.1).

682 Gates, W. L., and Coauthors, 1999: An Overview of the Results of the Atmospheric Model  
683 Intercomparison Project (AMIP I). *Bulletin of the American Meteorological Society*, **80** (1),  
684 29–56, [https://doi.org/10.1175/1520-0477\(1999\)080<0029:AOOTRO>2.0.CO;2](https://doi.org/10.1175/1520-0477(1999)080<0029:AOOTRO>2.0.CO;2).

685 Gelaro, R., and Coauthors, 2017: The Modern-Era Retrospective Analysis for Research and  
686 Applications, Version 2 (MERRA-2). *Journal of Climate*, **30** (14), 5419–5454, <https://doi.org/10.1175/JCLI-D-16-0758.1>.

688 Govekar, P. D., C. Jakob, and J. Catto, 2014: The relationship between clouds and dynamics in  
689 Southern Hemisphere extratropical cyclones in the real world and a climate model. *Journal of*  
690 *Geophysical Research: Atmospheres*, **119** (11), <https://doi.org/10.1002/2013JD020699>.

691 Graff, L. S., and J. H. LaCasce, 2014: Changes in Cyclone Characteristics in Response to Modified  
692 SSTs. *Journal of Climate*, **27** (11), 4273–4295, <https://doi.org/10.1175/JCLI-D-13-00353.1>.

693 Grise, K. M., and M. K. Kelleher, 2021: Midlatitude Cloud Radiative Effect Sensitivity to Cloud  
694 Controlling Factors in Observations and Models: Relationship with Southern Hemisphere Jet  
695 Shifts and Climate Sensitivity. *Journal of Climate*, **34**, 5869–5886, <https://doi.org/10.1175/JCLI-D-20-0986.1>.

697 Grise, K. M., and L. M. Polvani, 2014: Southern Hemisphere Cloud–Dynamics Biases in CMIP5  
698 Models and Their Implications for Climate Projections. *Journal of Climate*, **27** (15), 6074–6092,  
699 <https://doi.org/10.1175/JCLI-D-14-00113.1>.

700 Grose, M. R., J. S. Risbey, A. F. Moise, S. Osbrough, C. Heady, L. Wilson, and T. Erwin, 2016: Con-  
701 straints on Southern Australian Rainfall Change Based on Atmospheric Circulation in CMIP5  
702 Simulations. *Journal of Climate*, **30** (1), 225–242, <https://doi.org/10.1175/JCLI-D-16-0142.1>.

703 Gutjahr, O., D. Putrasahan, K. Lohmann, J. H. Jungclaus, J.-S. von Storch, N. Brüggemann,  
704 H. Haak, and A. Stössel, 2019: Max Planck Institute Earth System Model (MPI-ESM1.2)  
705 for the High-Resolution Model Intercomparison Project (HighResMIP). *Geoscientific Model*  
706 *Development*, **12** (7), 3241–3281, <https://doi.org/10.5194/gmd-12-3241-2019>.

707 Haarsma, R. J., and Coauthors, 2016: High Resolution Model Intercomparison Project (High-  
708 ResMIP v1.0) for CMIP6. *Geoscientific Model Development*, **9** (11), 4185–4208, <https://doi.org/10.5194/gmd-9-4185-2016>.

710 Hawcroft, M. K., L. C. Shaffrey, K. I. Hodges, and H. F. Dacre, 2012: How much Northern  
711 Hemisphere precipitation is associated with extratropical cyclones? *Geophysical Research*  
712 *Letters*, **39** (24), <https://doi.org/10.1029/2012GL053866>.

713 Hersbach, H., and Coauthors, 2020: The ERA5 global reanalysis. *Quarterly Journal of the Royal*  
714 *Meteorological Society*, **146** (730), 1999–2049, <https://doi.org/10.1002/qj.3803>.

715 Hodges, K. I., 1995: Feature Tracking on the Unit Sphere. *Monthly Weather Review*, **123** (12),  
716 3458–3465, [https://doi.org/10.1175/1520-0493\(1995\)123<3458:FTOTUS>2.0.CO;2](https://doi.org/10.1175/1520-0493(1995)123<3458:FTOTUS>2.0.CO;2).

717 Hodges, K. I., 1996: Spherical Nonparametric Estimators Applied to the UGAMP Model In-  
718 tegration for AMIP. *Monthly Weather Review*, **124** (12), 2914–2932, [https://doi.org/10.1175/1520-0493\(1996\)124<2914:SNEATT>2.0.CO;2](https://doi.org/10.1175/1520-0493(1996)124<2914:SNEATT>2.0.CO;2).

719

720 Hodges, K. I., 1999: Adaptive Constraints for Feature Tracking. *Monthly Weather Review*, **127** (6),  
721 1362–1373, [https://doi.org/10.1175/1520-0493\(1999\)127<1362:ACFFT>2.0.CO;2](https://doi.org/10.1175/1520-0493(1999)127<1362:ACFFT>2.0.CO;2).

722 Hodges, K. I., R. W. Lee, and L. Bengtsson, 2011: A Comparison of Extratropical Cyclones  
723 in Recent Reanalyses ERA-Interim, NASA MERRA, NCEP CFSR, and JRA-25. *Journal of*  
724 *Climate*, **24** (18), 4888–4906, <https://doi.org/10.1175/2011JCLI4097.1>.

725 Hyder, P., and Coauthors, 2018: Critical Southern Ocean climate model biases traced to atmo-  
726 spheric model cloud errors. *Nature Communications*, **9** (1), 3625.

727 Inatsu, M., and B. J. Hoskins, 2004: The Zonal Asymmetry of the Southern Hemisphere Winter  
728 Storm Track. *Journal of Climate*, **17** (24), 4882–4892, <https://doi.org/10.1175/JCLI-3232.1>.

729 Inatsu, M., and B. J. Hoskins, 2006: The Seasonal and Wintertime Variability of the Split Jet and  
730 the Storm-Track Activity Minimum Near New Zealand. *J. Meteor. Soc. Japan*, **84** (3), 433–445,  
731 <https://doi.org/https://doi.org/10.2151/jmsj.84.433>.

732 James, I. N., 1988: On the forcing of planetary-scale Rossby waves by Antarctica. *Quarterly*  
733 *Journal of the Royal Meteorological Society*, **114** (481), 619–637, <https://doi.org/10.1002/qj.49711448105>.

734

735 Kajtar, J. B., A. Santoso, M. Collins, A. S. Taschetto, M. H. England, and L. M. Frankcombe,  
736 2021: CMIP5 Intermodel Relationships in the Baseline Southern Ocean Climate System and

- 737 With Future Projections. *Earth's Future*, **9** (6), e2020EF001 873, [https://doi.org/https://doi.org/](https://doi.org/https://doi.org/10.1029/2020EF001873)  
738 10.1029/2020EF001873.
- 739 Kaspi, Y., and T. Schneider, 2013: The Role of Stationary Eddies in Shaping Midlatitude  
740 Storm Tracks. *Journal of the Atmospheric Sciences*, **70** (8), 2596–2613, [https://doi.org/](https://doi.org/10.1175/JAS-D-12-082.1)  
741 10.1175/JAS-D-12-082.1.
- 742 Kawai, H., S. Yukimoto, T. Kosshiro, N. Oshima, T. Tanaka, H. Yoshimura, and R. Nagasawa, 2019:  
743 Significant improvement of cloud representation in the global climate model mri-esm2. *Geo-*  
744 *scientific Model Development*, **12** (7), 2875–2897, <https://doi.org/10.5194/gmd-12-2875-2019>,  
745 URL <https://www.geosci-model-dev.net/12/2875/2019/>.
- 746 Kidston, J., and E. P. Gerber, 2010: Intermodel variability of the poleward shift of the austral  
747 jet stream in the CMIP3 integrations linked to biases in 20th century climatology. *Geophysical*  
748 *Research Letters*, **37** (9), <https://doi.org/10.1029/2010GL042873>.
- 749 Kobayashi, S., and Coauthors, 2015: The JRA-55 Reanalysis: General Specifications and Basic  
750 Characteristics. *Journal of the Meteorological Society of Japan*, **93** (1), 5–48, [https://doi.org/](https://doi.org/10.2151/jmsj.2015-001)  
751 10.2151/jmsj.2015-001.
- 752 Lee, R. W., 2015: Storm track biases and changes in a warming climate from an extratropical  
753 cyclone perspective using CMIP5. Ph.D. thesis, University of Reading.
- 754 Li, Y., D. W. J. Thompson, and S. Bony, 2015: The Influence of Atmospheric Cloud Radiative  
755 Effects on the Large-Scale Atmospheric Circulation. *Journal of Climate*, **28** (18), 7263–7278,  
756 <https://doi.org/10.1175/JCLI-D-14-00825.1>.
- 757 Lindsay, R., M. Wensnahan, A. Schweiger, and J. Zhang, 2014: Evaluation of Seven Differ-  
758 ent Atmospheric Reanalysis Products in the Arctic. *Journal of Climate*, **27** (7), 2588–2606,  
759 <https://doi.org/10.1175/JCLI-D-13-00014.1>.
- 760 Loeb, N. G., and Coauthors, 2018: Clouds and the Earth's Radiant Energy System (CERES) Energy  
761 Balanced and Filled (EBAF) Top-of-Atmosphere (TOA) Edition-4.0 Data Product. *Journal of*  
762 *Climate*, **31** (2), 895–918, <https://doi.org/10.1175/JCLI-D-17-0208.1>.

- 763 Mauritsen, T., and Coauthors, 2019: Developments in the MPI-M Earth System Model version 1.2  
764 (MPI-ESM1.2) and Its Response to Increasing CO<sub>2</sub>. *Journal of Advances in Modeling Earth*  
765 *Systems*, **11** (4), 998–1038, <https://doi.org/10.1029/2018MS001400>.
- 766 Meehl, G. A., C. Covey, T. Delworth, M. Latif, B. McAvaney, J. F. B. Mitchell, R. J. Stouffer, and  
767 K. E. Taylor, 2007: The WCRP CMIP3 Multimodel Dataset: A New Era in Climate Change  
768 Research. *Bulletin of the American Meteorological Society*, **88** (9), 1383 – 1394, [https://doi.org/](https://doi.org/10.1175/BAMS-88-9-1383)  
769 [10.1175/BAMS-88-9-1383](https://doi.org/10.1175/BAMS-88-9-1383).
- 770 Menary, M. B., D. L. R. Hodson, J. I. Robson, R. T. Sutton, R. A. Wood, and J. A. Hunt, 2015:  
771 Exploring the impact of CMIP5 model biases on the simulation of North Atlantic decadal  
772 variability. *Geophysical Research Letters*, **42** (14), 5926–5934, [https://doi.org/https://doi.org/](https://doi.org/https://doi.org/10.1002/2015GL064360)  
773 [10.1002/2015GL064360](https://doi.org/10.1002/2015GL064360).
- 774 Met Office, 2010 - 2013: *Iris: A Python library for analysing and visualising meteorological and*  
775 *oceanographic data sets*. Exeter, Devon, v1.2 ed., URL <http://scitools.org.uk/>.
- 776 Mooney, P. A., F. J. Mulligan, and R. Fealy, 2011: Comparison of ERA-40, ERA-Interim and  
777 NCEP/NCAR reanalysis data with observed surface air temperatures over Ireland. *International*  
778 *Journal of Climatology*, **31** (4), 545–557, <https://doi.org/10.1002/joc.2098>.
- 779 Nakamura, H., T. Sampe, A. Goto, W. Ohfuchi, and S.-P. Xie, 2008: On the importance of  
780 midlatitude oceanic frontal zones for the mean state and dominant variability in the tropospheric  
781 circulation. *Geophysical Research Letters*, **35** (15), <https://doi.org/10.1029/2008GL034010>.
- 782 Nakayama, M., H. Nakamura, and F. Ogawa, 2021: Impacts of a Midlatitude Oceanic Frontal Zone  
783 for the Baroclinic Annular Mode in the Southern Hemisphere. *Journal of Climate*, [https://doi.org/](https://doi.org/10.1175/JCLI-D-20-0359.1)  
784 [10.1175/JCLI-D-20-0359.1](https://doi.org/10.1175/JCLI-D-20-0359.1).
- 785 Nie, Y., Y. Zhang, X.-Q. Yang, and H.-L. Ren, 2019: Winter and Summer Rossby Wave Sources  
786 in the CMIP5 Models. *Earth and Space Science*, **6** (10), 1831–1846, [https://doi.org/https://doi.org/](https://doi.org/https://doi.org/10.1029/2019EA000674)  
787 [//doi.org/10.1029/2019EA000674](https://doi.org/10.1029/2019EA000674).
- 788 Patterson, M., T. Bracegirdle, and T. Woollings, 2019: Southern Hemisphere Atmospheric Block-  
789 ing in CMIP5 and Future Changes in the Australia-New Zealand Sector. *Geophysical Research*  
790 *Letters*, **0** (0), <https://doi.org/10.1029/2019GL083264>.

- 791 Patterson, M., T. Woollings, T. Bracegirdle, and N. T. Lewis, 2020: Wintertime Southern Hemi-  
792 sphere jet streams shaped by interaction of transient eddies with Antarctic orography. *Journal*  
793 *of Climate*, 1–57, <https://doi.org/10.1175/JCLI-D-20-0153.1>.
- 794 Pithan, F., T. G. Shepherd, G. Zappa, and I. Sandu, 2016: Climate model biases in jet streams,  
795 blocking and storm tracks resulting from missing orographic drag. *Geophysical Research Letters*,  
796 **43 (13)**, 7231–7240, <https://doi.org/10.1002/2016GL069551>.
- 797 Priestley, M. D. K., D. Ackerley, J. L. Catto, and K. I. Hodges, 2022: Drivers of biases in the  
798 CMIP6 extratropical storm tracks. Part 1: Northern Hemisphere. *Journal of Climate*, 1–37,  
799 <https://doi.org/10.1175/JCLI-D-20-0976.1>.
- 800 Priestley, M. D. K., D. Ackerley, J. L. Catto, K. I. Hodges, R. E. McDonald, and R. W. Lee, 2020:  
801 An Overview of the Extratropical Storm Tracks in CMIP6 Historical Simulations. *Journal of*  
802 *Climate*, **33 (15)**, 6315–6343, <https://doi.org/10.1175/JCLI-D-19-0928.1>.
- 803 Roberts, M. J., and Coauthors, 2019: Description of the resolution hierarchy of the global coupled  
804 HadGEM3-GC3.1 model as used in CMIP6 HighResMIP experiments. *Geoscientific Model*  
805 *Development*, **12 (12)**, 4999–5028, <https://doi.org/10.5194/gmd-12-4999-2019>.
- 806 Sallée, J.-B., E. Shuckburgh, N. Bruneau, A. J. S. Meijers, T. J. Bracegirdle, Z. Wang, and T. Roy,  
807 2013: Assessment of Southern Ocean water mass circulation and characteristics in CMIP5  
808 models: Historical bias and forcing response. *Journal of Geophysical Research: Oceans*,  
809 **118 (4)**, 1830–1844, <https://doi.org/10.1002/jgrc.20135>.
- 810 Sandu, I., and Coauthors, 2019: Impacts of orography on large-scale atmospheric circulation. *npj*  
811 *Climate and Atmospheric Science*, **2 (1)**, 10.
- 812 Stouffer, R. J., V. Eyring, G. A. Meehl, S. Bony, C. Senior, B. Stevens, and K. E. Taylor, 2017:  
813 CMIP5 Scientific Gaps and Recommendations for CMIP6. *Bulletin of the American Meteorolo-*  
814 *gical Society*, **98 (1)**, 95–105, <https://doi.org/10.1175/BAMS-D-15-00013.1>.
- 815 Tamarin, T., and Y. Kaspi, 2016: The Poleward Motion of Extratropical Cyclones from a Po-  
816 tential Vorticity Tendency Analysis. *Journal of the Atmospheric Sciences*, **73 (4)**, 1687–1707,  
817 <https://doi.org/10.1175/JAS-D-15-0168.1>.

818 Taylor, K. E., R. J. Stouffer, and G. A. Meehl, 2012: An Overview of CMIP5 and the Experiment  
819 Design. *Bulletin of the American Meteorological Society*, **93** (4), 485–498, [https://doi.org/](https://doi.org/10.1175/BAMS-D-11-00094.1)  
820 10.1175/BAMS-D-11-00094.1.

821 Taylor, K. E., and Coauthors, 2017: CMIP6 Global Attributes, DRS, Filenames, Directory Structure  
822 and, CV's. Tech. Rep. v6.2.6, Program for Climate Model Diagnosis and Intercomparison,  
823 <http://goo.gl/v1drZl>.

824 Tian, B., and X. Dong, 2020: The Double-ITCZ Bias in CMIP3, CMIP5, and CMIP6 Models  
825 Based on Annual Mean Precipitation. *Geophysical Research Letters*, **47** (8), e2020GL087232,  
826 <https://doi.org/10.1029/2020GL087232>.

827 Trenberth, K. E., and J. T. Fasullo, 2010: Simulation of Present-Day and Twenty-First-Century  
828 Energy Budgets of the Southern Oceans. *Journal of Climate*, **23** (2), 440–454, [https://doi.org/](https://doi.org/10.1175/2009JCLI3152.1)  
829 10.1175/2009JCLI3152.1.

830 Trenberth, K. E., J. T. Fasullo, and J. Mackaro, 2011: Atmospheric Moisture Transports from  
831 Ocean to Land and Global Energy Flows in Reanalyses. *Journal of Climate*, **24** (18), 4907–  
832 4924, <https://doi.org/10.1175/2011JCLI4171.1>.

833 Tsujino, H., and Coauthors, 2020: Evaluation of global ocean–sea-ice model simulations based on  
834 the experimental protocols of the Ocean Model Intercomparison Project phase 2 (OMIP-2). *Geo-*  
835 *scientific Model Development*, **13** (8), 3643–3708, <https://doi.org/10.5194/gmd-13-3643-2020>.

836 Voigt, A., and T. A. Shaw, 2015: Circulation response to warming shaped by radiative changes of  
837 clouds and water vapour. *Nature Geoscience*, **8**, 102–106, <https://doi.org/10.1038/ngeo2345>.

838 Wang, C., L. Zhang, S.-K. Lee, L. Wu, and C. R. Mechoso, 2014: A global perspective on  
839 CMIP5 climate model biases. *Nature Climate Change*, **4** (3), 201–205, [https://doi.org/10.1038/](https://doi.org/10.1038/nclimate2118)  
840 nclimate2118.

841 Wilcox, L. J., A. J. Charlton-Perez, and L. J. Gray, 2012: Trends in Austral jet position in ensembles  
842 of high- and low-top CMIP5 models. *Journal of Geophysical Research: Atmospheres*, **117** (D13),  
843 <https://doi.org/10.1029/2012JD017597>.

- 844 Williams, K. D., and A. Bodas-Salcedo, 2017: A multi-diagnostic approach to cloud  
845 evaluation. *Geoscientific Model Development*, **10** (7), 2547–2566, [https://doi.org/10.5194/](https://doi.org/10.5194/gmd-10-2547-2017)  
846 [gmd-10-2547-2017](https://doi.org/10.5194/gmd-10-2547-2017).
- 847 Williams, K. D., and Coauthors, 2013: The Transpose-AMIP II Experiment and Its Application  
848 to the Understanding of Southern Ocean Cloud Biases in Climate Models. *Journal of Climate*,  
849 **26** (10), 3258–3274, <https://doi.org/10.1175/JCLI-D-12-00429.1>.
- 850 Willison, J., W. A. Robinson, and G. M. Lackmann, 2013: The Importance of Resolving Mesoscale  
851 Latent Heating in the North Atlantic Storm Track. *Journal of the Atmospheric Sciences*, **70** (7),  
852 2234–2250, <https://doi.org/10.1175/JAS-D-12-0226.1>.
- 853 Wood, T., C. M. McKenna, A. Chrysanthou, and A. C. Maycock, 2020: Role of sea surface temper-  
854 ature patterns for the Southern Hemisphere jet stream response to CO2 forcing. *Environmental*  
855 *Research Letters*, **16** (1), 014 020, <https://doi.org/10.1088/1748-9326/abce27>.
- 856 Zelinka, M. D., T. A. Myers, D. T. McCoy, S. Po-Chedley, P. M. Caldwell, P. Ceppi, S. A. Klein,  
857 and K. E. Taylor, 2020: Causes of Higher Climate Sensitivity in CMIP6 Models. *Geophysical*  
858 *Research Letters*, **47** (1), e2019GL085 782, <https://doi.org/10.1029/2019GL085782>.